Chapter 3

Target System and Support Facility

3.1 Introduction

3.1.1 Overview

The role of the target system at a Neutrino Factory is to generate a maximal number of pions with an intense proton beam and then capture and guide them into a channel where the decay muons can be bunched, cooled, accelerated and stored in a ring from which the neutrinos emanate upon decay of the muons.

In this Study, the proton beam energy is 24 GeV, and the baseline beam power is 1 MW, upgradable to 4 MW.

The spectrum of pions from GeV protons interacting with a target peaks at a total momentum near 250 MeV/c, as shown in Fig. 3.1 [1], and has an average transverse momentum $\langle p_\perp \rangle = 150$ MeV/c. Thus, the majority of pions are produced at relatively large angles to the proton beam, and are not efficiently captured by devices placed downstream of the target. For maximal efficiency, the pion capture system must surround the target.

The capture mechanism considered here is a solenoidal magnetic field channel starting at 20 T near the target, then falling adiabatically to 1.25 T downstream ($\approx$ 18 m) from the target. This configuration creates a kind of magnetic bottle whose mouth is the muon phase rotation system considered in Chapter 4. In a solenoidal field the pion (and muon) trajectories are helices, with adiabatic invariants BR^2 and $p_\perp^2/B$. We propose to capture pions with $p_\perp \leq 225$ MeV/c, for which an aperture of 7.5 cm is required at 20 T. After the adiabatic reduction of the solenoid field by a factor of 16, to 1.25 T, the captured pions are contained within an aperture of 30 cm and have a maximum $p_\perp$ of 67.5 MeV/c.

For proton beam energies above about 8 GeV, the pion yield per proton increases

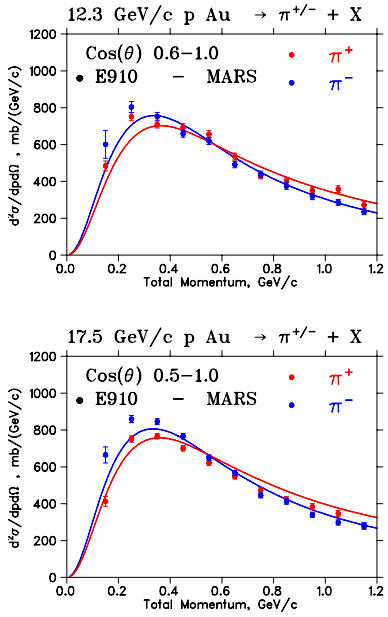

Figure 3.1: Momentum spectra for pion production by 12.3 and 17.5 GeV protons on a gold target, from BNL E910 and from MARS calculations.

with the atomic number of the target, as shown in Fig. 3.2 from a MARS calculation [2]. For 24 GeV protons, a high-Z target is distinctly superior in yield [3].

As the pions to be captured emerge from the target at large angles to the beam, and follow helical paths that may intersect the target at more than one point, it is advantageous for the target to be in the form of a narrow rod, tilted at a small angle to the magnetic axis. As shown in Fig. 3.3, suitable parameters for a mercury target in a 20 T solenoid are a tilt angle of 100 mrad and a target radius of 5 mm.

In a 1 MW beam with 15 pulses per second, each pulse contains 60 kJ energy, of which about 10% is deposited in a two-interaction-length high-Z target. The energy deposited in the target will heat the target to a temperature of several hundred °C and generate substantial shock pressures. A low-Z target, as proposed in Study-I [4], is expected to survive these shocks for a significant time with a 1.5 MW beam, but is predicted to have a pion production yield only half that of high-Z targets, such as Inconel, or mercury. It would also be expected to get too hot with a 4 MW beam, which we consider to be a likely upgrade. A liquid-mercury-jet target, too, will be disrupted by the heating from the beam, but such disruption is not expected to have significant adverse consequences,

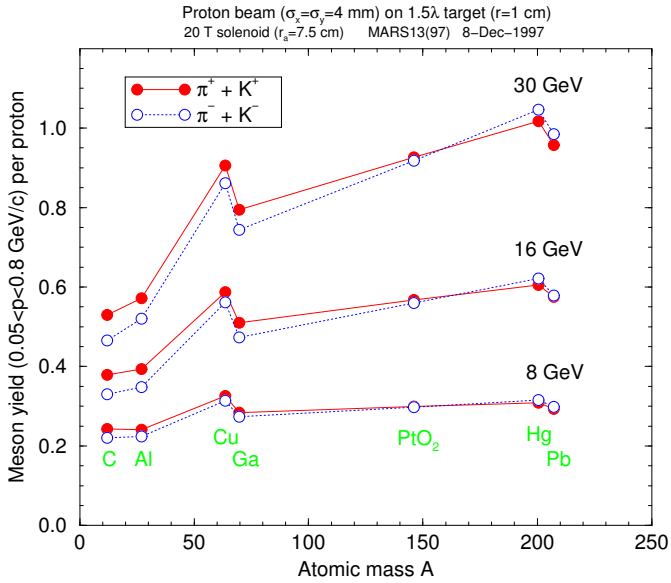

Figure 3.2: Pion yield *vs.* atomic mass number of the target at three proton beam energies.

even at 4 MW. For this reason, a mercury-jet target has been selected as the baseline for this study. If there were advantages to doing so, liquids such as a molten lead/tin eutectic, or other alloys, could be used. A graphite target (as considered in Study-I) would be available as a backup, though it would reduce the neutrino intensity by a factor of 1.9 (see [4], Section 3.5).

In this Study, the beam with rms radius σ_r, at a vertical angle θ_p, intersects the mercury jet of radius r_o and vertical angle $\theta_{\rm Hg}$ at an angle $\theta_{\rm crossing}$. The forward velocity of the jet is v_o.The nozzle is at $z_{\rm nozzle}$ with respect to the intersection of the beam and jet center lines. The interval between pulses is t. The Study-II baseline values of these parameters are given in Table 3.1.

An alternative target concept based on a rotating Inconel band is discussed in [5].

3.1.2 Target System Layout

The target system consists of the following components:

- Target enclosure vessel

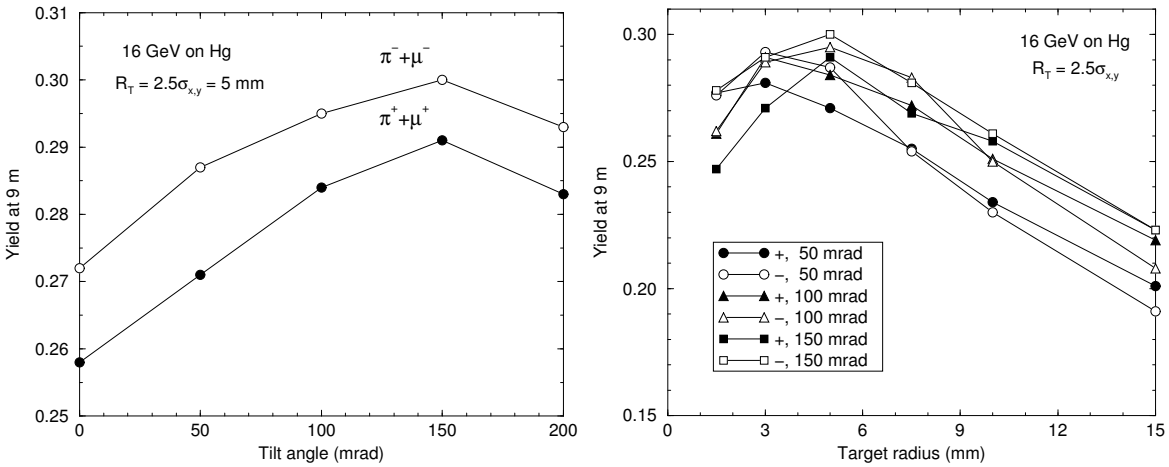

Figure 3.3: Pion yield from Hg targets *vs.* tilt angle angle between the target/beam axis and the solenoid axis (left) and *vs.* the radius of the target (right).

- Proton beam window
- Mercury jet, including its supply line within the enclosure vessel and the jet nozzle
- Magnet coils
- Internal shielding
- Mercury collection pool/dump and entrance baffle
- Downstream window

The overall layout of the target area is sketched in Fig. 3.4, with a detail of the target region shown at the bottom of Fig. 3.5. The intersection of the beam and jet is set at 45 cm from the nozzle. The distribution of the resulting interactions as a function of z, shown at the top of Fig. 3.5, starts about 15 cm from the nozzle.

It will be assumed here that, after a pulse, all the mercury outside of the nozzle is dispersed. This is predicted using the finite element analysis code FronTier [6], as illustrated in Fig. 3.6. At the arrival time of a subsequent bunch, the newly established jet will extend a distance $\Delta z = v_o\, t = 0.6$ m from the nozzle. Only 2.5% of the interactions occur beyond this location, so the disposition of the disturbed jet beyond this point has little effect on production.

Table 3.1: Proton beam and mercury jet geometric parameters.

Beam σ_r (mm)	1.5
Beam angle to magnet axis θ_p (mrad)	-67
Jet material	mercury
Velocity v_o (m/s)	30
Jet radius r_o (mm)	5
Jet angle to magnet axis $\theta_{\rm Hg}$ (mrad)	-100
Crossing angle $\theta_{\rm crossing}$ (mrad)	33
t between bunches (ms)	20
$z_{\rm nozzle}$ (cm)	-60

The distance over which the jet must propagate without serious magnetic disruption is from the nozzle to a point 0.6 m downstream, defined as $z = 0$ in the coordinate system used here. In order to minimize the field nonuniformity over this length, the magnetic center (approximately the point of maximum B_z) is placed at the center of this length. *i.e.*, the magnetic center is at $z_o = -30$ cm. The intersection of the jet and beam is then at $z_{\rm intersection} = -15$ cm, and the nozzle is at $z_{\rm nozzle} = -60$ cm.

3.1.3 Capture and Matching Solenoids

The target is located in a 20 T solenoid to contain transverse momenta of outcoming pions up to 225 MeV/c, a large fraction of all pions produced. The central region of high field is designed to be uniform, drooping only 5% at its end, to limit the magnetic field gradients that might disrupt the mercury jet. The solenoid is a hybrid, with copper inner coils and superconducting outer coils. It is similar to that discussed in Feasibility Study-I [4]. However, here we use hollow copper conductor for the inner coils, rather than a Bitter-style magnet. This choice is aimed at achieving a magnet life over 40 years (compared with 6 months in Study-I), and avoiding possible corrosion problems with the highly irradiated wet insulation in a Bitter magnet. The main disadvantage of this choice is that it consumes more power and requires a greater field contribution from the SC coils..

Downstream of the 20 T magnet, additional superconducting coils taper the axial field down smoothly to 1.25 T over a distance of approximately 18 m, according to the form,

$$B(z) \;\approx\; \frac{B(0)\ \mathrm{T}}{1 + k\ z}\,. \tag{3.1}$$

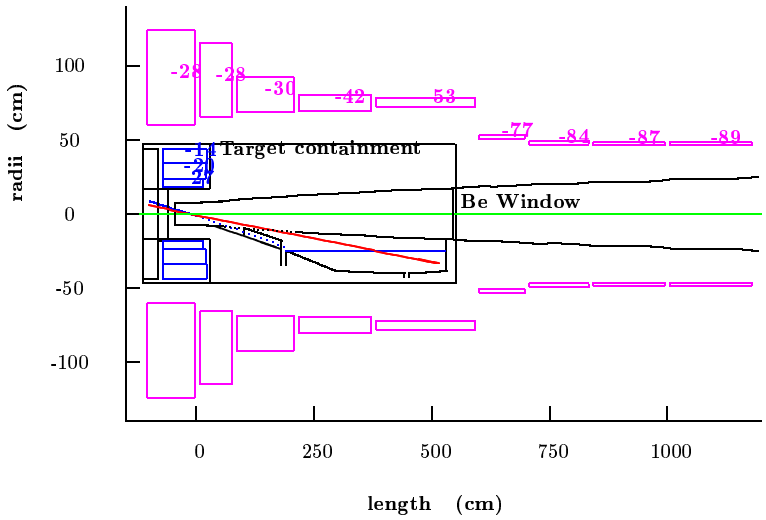

Figure 3.4: Target, capture solenoids and mercury containment.

Dimensions of the coils and the upstream iron pole are given in Table 3.2. The coils are shown in Fig. 3.4, and axial field profiles, over two scales of z, are shown in Fig. 3.8.

3.1.4 Magnetic Disruption of the Mercury Jet

As the jet moves through the magnet, eddy currents are induced in the mercury, and the resulting $\mathbf{J} \times \mathbf{B}$ force distorts the jet in various ways [7, 8]. Assuming a Gaussian distribution of B'_z *vs.* z' with a maximum value of B_o, where the z' axis is along the jet, jet conductivity κ, density ρ, and surface tension T_{surface} as given in Table 3.3, perturbation calculations [7] show that, over the extent of the jet from -0.6 to 0.0 m,

- The maximum axial field deviations are ± 1.1 T, *i.e.*, $\pm 5\%$.
- The axial pressure difference has a minimum of -0.25 atm. Thus, if the jet is operating in a gas (He or Ar) at a pressure greater than or equal to 0.25 atm, negative pressures will be avoided, and there will be no tendency to cavitate prior to the arrival of the beam.
- The maximum axial velocity change of the jet, 0.06 m/s, is very small compared with the average jet velocity, 30 m/s.

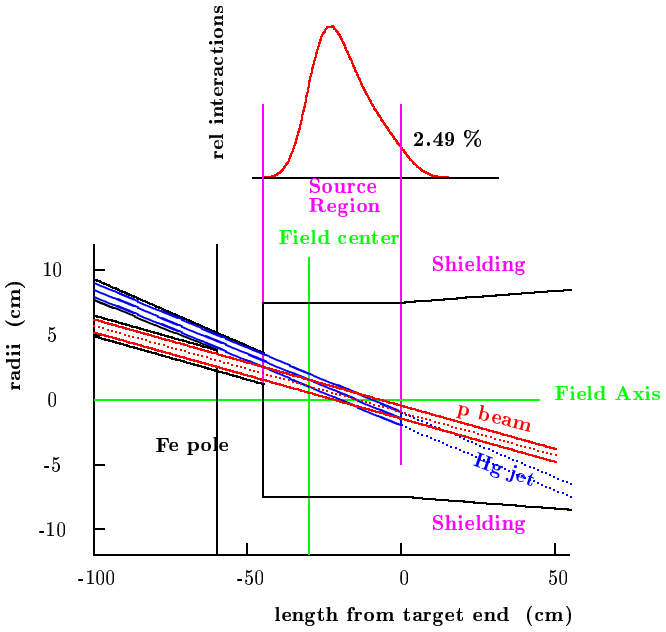

Figure 3.5: Top: Distribution of beam-target interactions as a function of z. Bottom: Layout of the target area.

- The maximum transverse velocity, 0.4 m/s, induced by shear forces is also small compared with the average jet velocity: $0.4/30 \approx 1.3\%$.
- The deflection of the jet, 5 μm, is very small.
- The transverse distortion of the jet (change in width relative to average width) is approximately 0.4% ignoring surface tension, and less than 0.2% when surface tension is included.

These disruptions are all relatively small, and should cause no problems for the beam-jet interaction.

Beyond the target region ($z > 0$), the magnetic effects are larger, but still not sufficient to break up the jet. Here, the maximum shear is about 5 m/s, and the transverse distortion 20%. However, since the beam-jet interaction will disperse the jet, a more significant effect thereafter is magnetic damping of the dispersal.

More detailed magnetohydrodynamic calculations are under way [6] using the FronTier 3-D finite element analysis code that includes liquid-gas boundaries and phase tran-

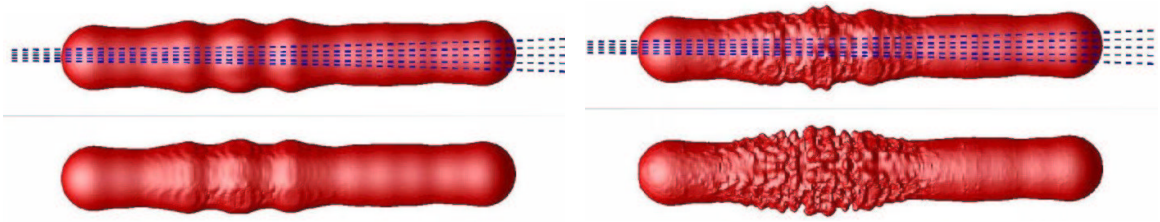

Figure 3.6: Beam-induced breakup of a mercury jet, as simulated by the FronTier code. The images are for 10 μs time steps.

sitions. Preliminary results are shown in Fig. 3.9.

A magnetic field also provides a desirable damping of oscillations of a mercury jet, with a time constant of roughly 100 μs. Figure 3.10 shows this effect in a recent study by a CERN/Grenoble collaboration as part of their Neutrino Factory R&D program.

3.1.5 Mercury Containment

Figure 3.4 also shows the concepts for the mercury containment vessel and the mercury pool beam dump, and Fig. 3.11 shows more detail. The containment vessel and dump are to be replacable, for which the hollow conductor coils must also be removed.

The mercury jet, or what remains of it, falls under gravity, and thus further separates from the beam axis. A system of grids or baffles slows the mercury spray before it joins the beam dump mercury pool. The outflow pipe is 10 cm in diameter to accommodate the considerable rate of filling from the jet. The drain would be opened only when emptying the contaiment vessel for its removal.

3.1.6 Target System Support Facility

The Target Support Facility consists of the target region and decay channel, a crane hall over the length of the facility, a maintenance cell at the ground floor elevation for handling magnet components, a hot cell at the tunnel level for mercury target system components, and various remote-handling equipment used for maintenance tasks. The facility is bounded by the proton beam window at the upstream end and the first induction linear accelerator at the downstream end. It contains the equipment for the mercury-jet target, high-field resistive and superconducting solenoids, low-field superconducting solenoids, water-cooled shielding to limit radiation dose and neutron heating to the coils, shielding to protect personnel and the environment, and a 50-ton crane that

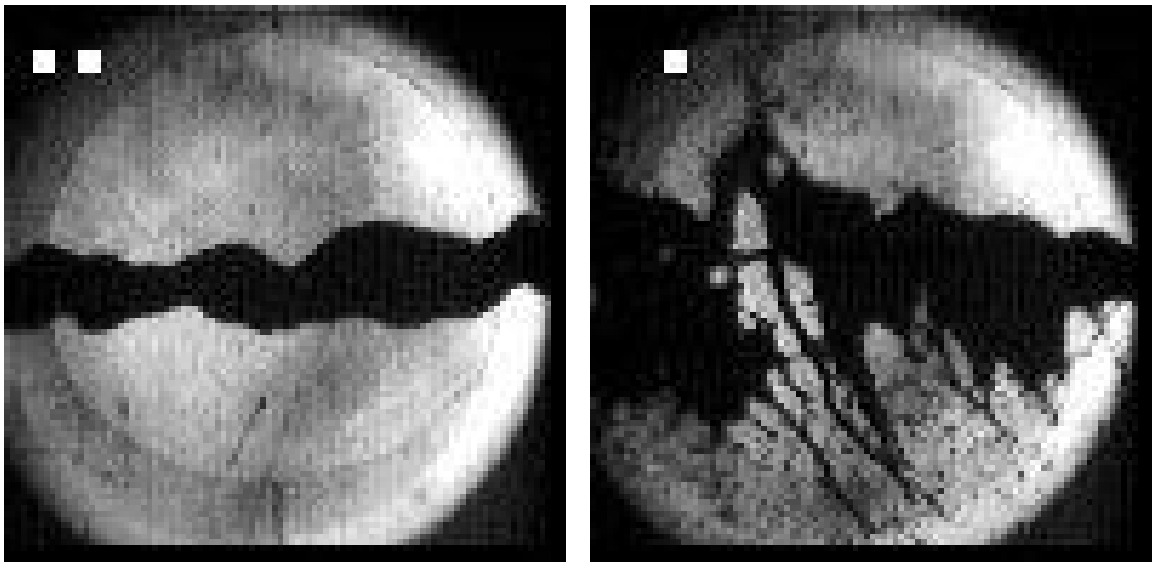

Figure 3.7: Breakup of a 1-cm-diameter mercury jet in a 24-GeV proton beam (BNL E951).

is used for the initial assembly and installation of major components and for subsequent maintenance activities. The target support facility is 12 m wide, and approximately 50 m long. Figure 3.12 is a view of the overall facility looking downstream.

The remainder of this section presents a conceptual design for the target caputure magnet, the mercury-jet target system, the proton-beam absorber, and the facility for the target/capture region.

3.2 Calculations of Pion Yield and Radiation Dose Using MARS

Detailed MARS14(2000) [9, 10] simulations have been performed for the optimized Study-II target-capture system configuration. A 24-GeV kinetic energy proton beam ($\sigma_x = \sigma_y =$ 1.5 mm, $\sigma_z = 3$ ns, 67 mrad) interacts with a 5 mm radius mercury jet tilted by 100 mrad, which is ejected from the nozzle at $z = -60$ cm, crosses the z-axis at $z = 0$ cm, and hits a mercury pool at $z = 220$ cm, $x = -25$ cm.

Results [11] are based on two runs of 400,000 protons on target each, including energy

Table 3.2: Solenoid coil geometric parameters.

	z (m)	Gap (m)	Δz (m)	R_i (m)	ΔR (m)	I/A (A/mm^2)	nI (A)	nIl (A-m)
Fe	0.980	0.980	0.108	0.000	0.313	0.00	0.00	0.00
	1.088	0.000	0.312	0.000	0.168	0.00	0.00	0.00
Cu coils	1.288	−0.112	0.749	0.178	0.054	24.37	0.98	1.26
	1.288	−0.749	0.877	0.231	0.122	19.07	2.04	3.74
	1.288	−0.877	1.073	0.353	0.137	14.87	2.18	5.78
SC coils	0.747	−1.614	1.781	0.636	0.642	23.39	26.77	160.95
	2.628	0.100	0.729	0.686	0.325	25.48	6.04	32.23
	3.457	0.100	0.999	0.776	0.212	29.73	6.29	34.86
	4.556	0.100	1.550	0.776	0.107	38.26	6.36	33.15
	6.206	0.100	1.859	0.776	0.066	49.39	6.02	30.59
	8.000	−0.065	0.103	0.416	0.051	68.32	0.36	1.00
	8.275	0.172	2.728	0.422	0.029	69.27	5.42	14.88
	11.053	0.050	1.749	0.422	0.023	75.62	3.00	8.18
	12.852	0.050	1.750	0.422	0.019	77.37	2.61	7.09
	14.652	0.050	1.749	0.422	0.017	78.78	2.30	6.22
	16.451	0.050	1.750	0.422	0.015	79.90	2.07	5.59
	18.251	0.050	2.366	0.422	0.013	-0.85	2.53	6.80

deposition in the mercury jet, the yield of captured pions, fluxes of charged and neutral particles and the consequent radiation dose in the materials of the target system. For example, the total power dissipation in the jet at $-60 < z < 0$ cm is 100 kW for 6 bunches at 2.5 Hz and 1.7×10^{13} protons per bunch. Preliminary results were given in Refs. [4, 3].

As noted earlier, to be conservative, we estimate radiation effects based on 2×10^7 s per operating year, though we estimate physics production based on a standard 1×10^7 s year.

3.2.1 Captured π/μ Beam *vs.* Target and Beam Parameters

Realistic 3-D geometry based on Fig. 3.4, together with material and magnetic field distributions based on the solenoid magnet design optimization, have been implemented into MARS. The level of detail in the model is illustrated by Fig. 3.13, which shows a

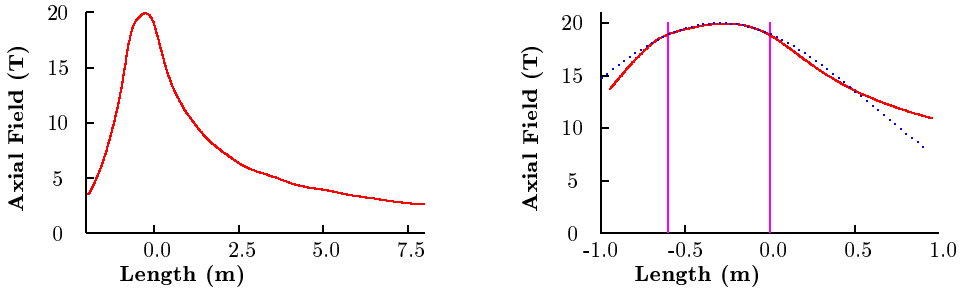

Figure 3.8: The axial magnetic field (solid lines) *vs.* length along the axis, on two scales. The dotted line is a Gaussian fit, with $\sigma_z = 0.8$ m, to the field in the jet region.

Table 3.3: Relevant properties of the mercury jet.

B_o (T)	20
σ'_z (m)	0.8
κ (Ω-m)	10^6
ρ (kg/m^3)	1.35×10^5
$T_{\rm surface}$ (N/m)	0.456

transverse section at $z = 5.2$ m that includes the mercury pool that serves as the proton beam absorber.

The use of a 3-D magnetic field map results in the reduction of the π/μ-yield in the decay channel by about 7% for C and by 10-14% for Hg targets, compared with the assumption that $B_z(r, z)$ obeys Eq. (3.1).

Both graphite (C) and mercury (Hg) tilted targets were studied. A two-interaction-length target (80 cm for C of radius $R_T = 7.5$ mm, and 30 cm for Hg of $R_T = 5$ mm) is found to be optimal in most cases, and we keep $R_T \geq 2.5\ \sigma_{x,y}$, where $\sigma_{x,y}$ are the beam rms spot sizes.

Results of a detailed optimization of the particle yield Y are presented below, in most cases for a sum of the numbers of π and μ of a given sign and energy interval at a fixed distance $z = 9$ m from the target. For proton energies E_p from a few GeV to about 30 GeV, the shape of the low-momentum spectrum of such a sum is energy-independent and peaks around 250 MeV/c momentum (145 MeV kinetic energy), as illustrated in Fig. 3.1. Moreover, the sum is practically independent of z at $z \geq 9$ m–confirming

Figure 3.9: Disruption of a mercury jet on entering and exiting a solenoid magnet, as simulated by the FronTier code.

a good matching and capturing–with a growing number of muons and proportionately decreasing number of pions along the decay channel. For the given parameters, the π/μ kinetic energy interval of 30 MeV $\leq E \leq$ 230 MeV, around the spectrum maximum is considered as the one to be captured by the downstream phase rotation system.

The yield Y grows with the proton energy E_p, is almost material-independent at low energies and grows with target A at high energies, being almost a factor of two higher for Hg than for C at E_p=16-30 GeV (Fig. 3.2). To avoid absorption of spiraling pions by target material, the target and beam are tilted by an angle α with respect to the solenoid axis. The yield is higher by 10-30% for the tilted target. For a short Hg target, α=150 mrad seems to be the optimum, as shown in Fig. 3.3 (left). The maximum yield occurs at target radius $R_T = 5$ mm for Hg with $R_T = 2.5\sigma_{x,y}$ (R_T=7.5 mm and $R_T = 3.5\sigma_{x,y}$ for C), as shown in Figs. 3.3 (right) and 3.14 (left). The yield with mercury could be further increased by increasing the target radius to gain secondary pion production, but the target heating would also be increased significantly, as shown in Fig. 3.14 (right).

Figure 3.15 shows longitudinal profiles of the energy density deposited in the mercury jet target in three radial regions. The center of the proton beam enters the jet at $z = -45$ cm, and the energy deposition peaks about 12 cm downstream of this point, at $z = -33$ cm.

3.2.2 Particle Fluxes, Power Density and Radiation Dose

Figure 3.16 shows the radiation per 2×10^7 s in the vicinity of the target. Table 3.4 gives the maximum doses per year and expected lifetime for various components (Note that for assessing radiation effects we take a larger operating year to be conservative).

Figures 3.17 and 3.18 illustrate charged and neutral particle fluxes, and the resulting

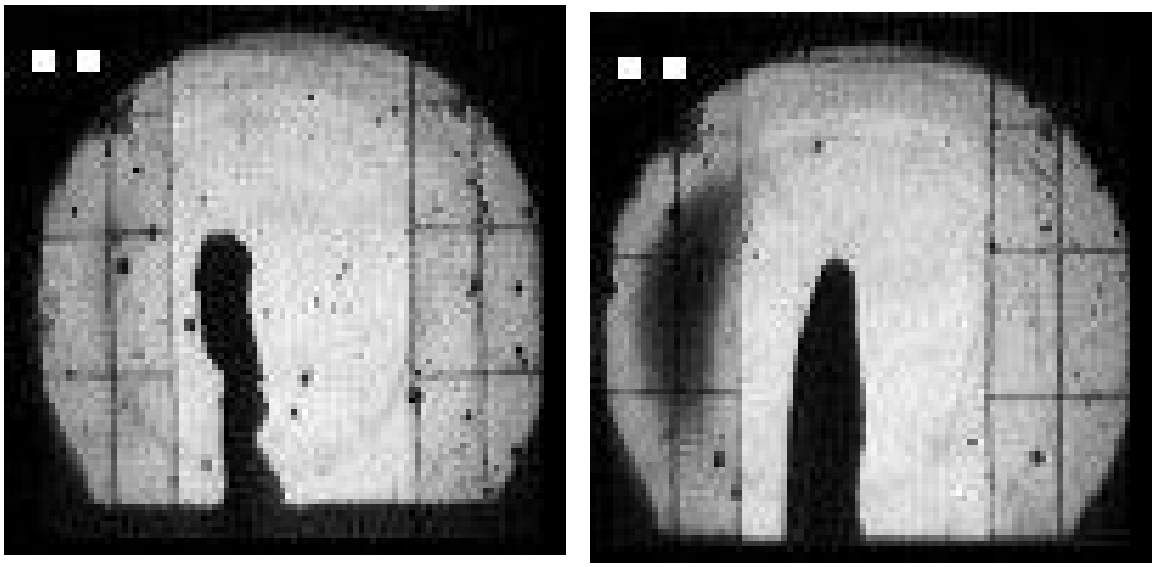

Figure 3.10: Magnetic damping of oscillations of a 1-cm-diameter, 4-m/s mercury jet in a 13-T solenoid magnet. Left: field off; right: field on.

power deposition and radiation dose, as a function of radius at the downstream end of the target. Figure 3.19 shows the power density and radiation dose in the beryllium window at $z = 6.1$ m.

The neutron flux in the target system is shown in Fig. 3.20, and the absorber radiation dose is shown in Figs. 3.16 and 3.21. Even at the end of the decay channel, at $z = 36$ m, the radiation levels remain high.

3.3 Calculations of Energy Deposition and Activation Using MCNPX

The energy deposition in, activation of, and radiation leakage from the target module have been estimated using the Monte Carlo code MCNPX [12]. This is a combination of the particle transport code MCNP-4B [13] and the high-energy transport code LAHET-2.8 [14]. This code employs a combinatorial surface/cell specification of the geometry, which permits modeling of the problem configuration with minimal approximations.

The MCNPX code has similar capabilities to those of the MARS code, although

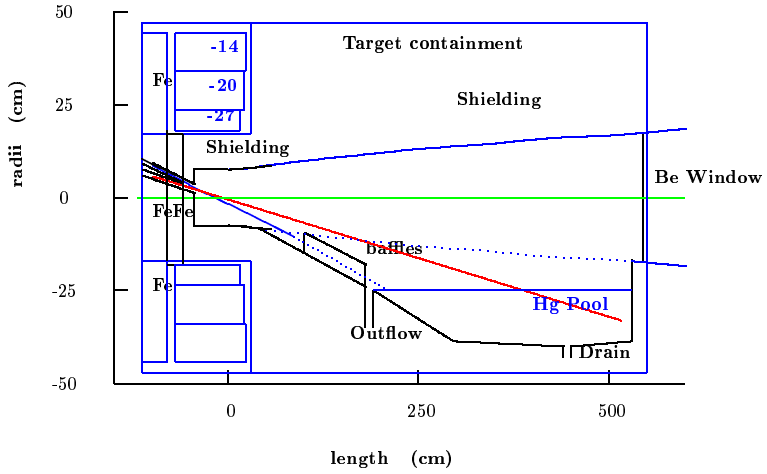

Figure 3.11: Beam dump, shielding and mercury containment detail.

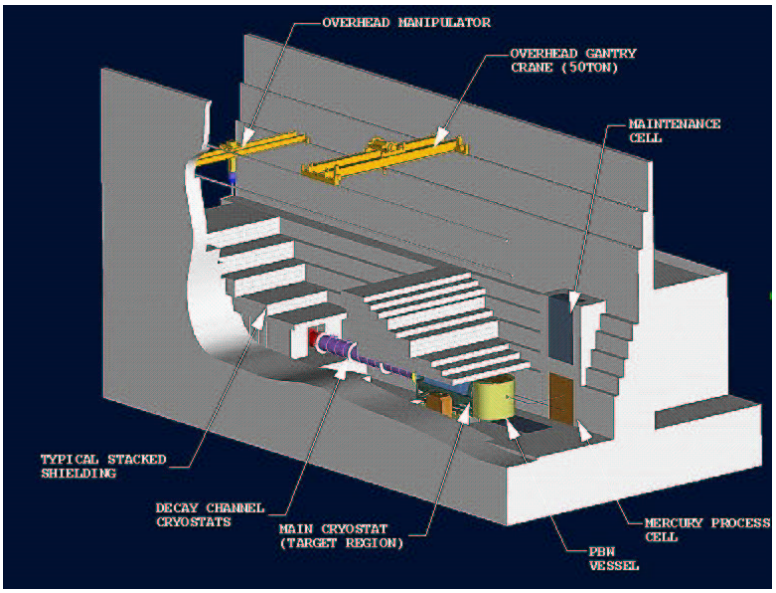

Figure 3.12: The overall target support facility.

MARS describes in great details the effects of magnetic field, capability that MCNPX is lacking. In addition, there are subtle differences in the way the geometry is represented

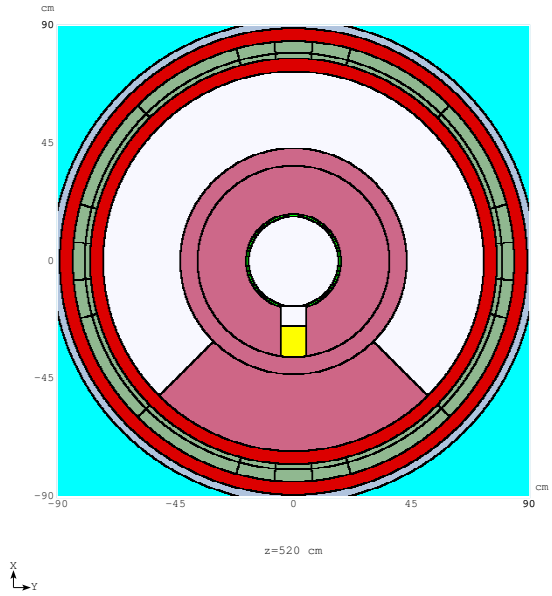

Figure 3.13: Transverse section of the target system at $z = 5.2$ m, showing the mercury pool that serves as the proton beam absorber.

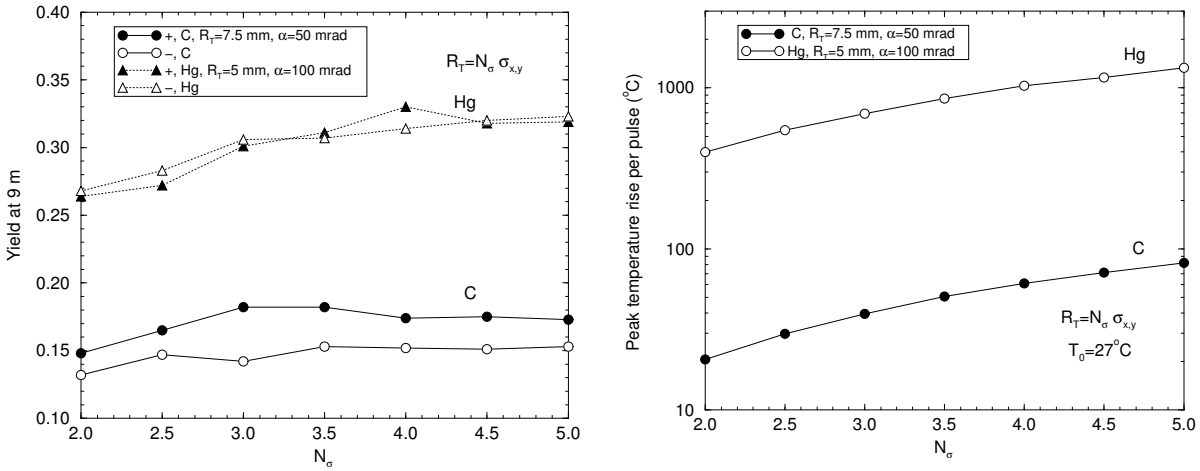

Figure 3.14: Pion yield (left) and maximum instantaneous temperature rise (right) as a function of the ratio of target radius to RMS beam spot size.

and nuclear data models are linked together, and the manner in which the activation

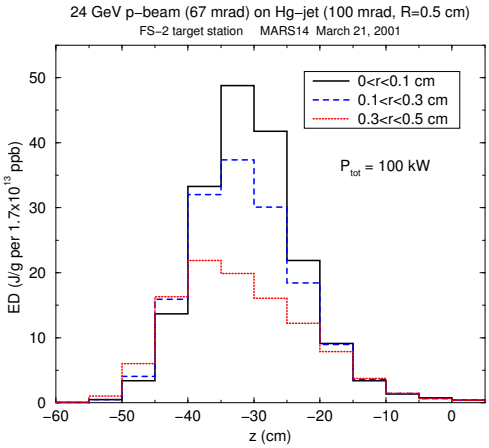

Figure 3.15: Longitudinal profiles of the energy density deposited in the mercury jet target in three radial regions.

and energy deposition analyses are carried out. Thus, the use of both codes provides important cross checks.

An appropriate model of the target module was created that includes the primary mercury jet, three surrounding magnets, the downstream shield structure, and a mercury beam stop. Two representative longitudinal and transverse sections through this model are shown in Figs. 3.22 and 3.23.

3.3.1 Energy Deposition

The energy deposition resulting from protons, neutrons, and photons is summarized in Table 3.5 in terms of MeV/gm-proton, as well as power density (W/cm^3) and total power per cell, assuming a 1-MW, 24-GeV proton beam.

The bulk of the beam power is deposited in the surrounding coaxial shield, the mercury jet target, and the coaxial shield surrounding the primary target (683 kW out of 1 MW). The total power deposited in the target module cells is 715 kW. The remaining 285 kW largely appears as radiation leakage out of the target system.

The two shield volumes are actively cooled by flowing water, and the above heat input sets the flow rate and the size of the heat exchanger. The iron plug immediately upstream of the primary target also requires active cooling, since it has a relatively high heat input. The magnets, of course, will be cooled actively. Finally, the mercury will be a flowing

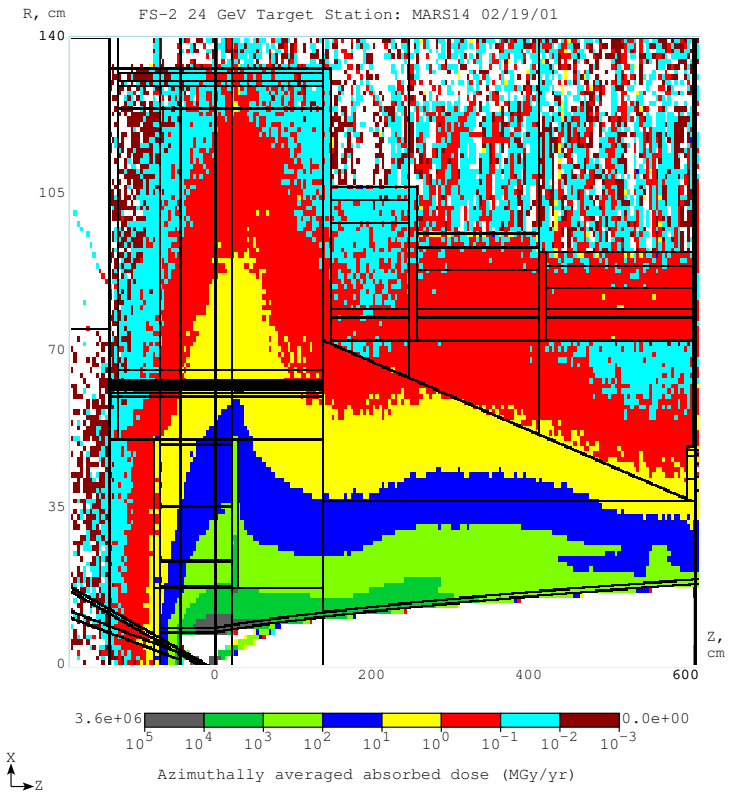

Figure 3.16: Absorbed radiation dose per year of 2×10^7 s and a 1 MW proton beam in the target system for $-2 < z < 6$ m and $r < 1.4$ m.

system, and the heat input determines the required capacity of the heat exchanger.

3.3.2 Activation Analysis

The activation analysis is based on the MCNPX estimates of neutron fluxes and spallation product masses. The neutron fluxes are used to determine cell-dependent activation cross sections, and the spallation mass distributions are used to determine the distribution of possible isotopes produced during the spallation reactions. The mass distributions are a function of cell type and position within the target module, since cells with the same composition in different positions are subject to different particle fluxes.

The time-dependent buildup of activation is based on the assumption of 100 days of

Table 3.4: Radiation doses and lifetimes of some components of the target system.

Component	Radius (cm)	Dose/yr (Grays/2×10^7 s)	Max allowed Dose (Grays)	1 MW Life (years)	4 MW life (years)
Inner shielding	7.5	2×10^{11}	10^{12}	5	1.25
Hg containment	18	2×10^9	10^{11}	50	12
Hollow conductor	18	1×10^9	10^{11}	100	25
Superconducting coil	65	6×10^6	10^8	16	4

Table 3.5: Energy deposition by cell in the target system. (x) stands for $\times 10^x$.

Cell Number	Description	Energy Deposition (Mev/gm-p)	(W/cm^3)	(kW)
8	Surrounding shield	3.11(-4)	0.16	589
12	Primary mercury target	2.62	1.48(3)	53.1
2	Coaxial shield around target	1.55(-3)	0.82	40.4
3	Iron plug behind target	1.21(-3)	0.39	0.99
81	First coaxial magnet	2.61(-4)	0.08	3.54
82	Second coaxial magnet	1.04(-4)	0.03	4.43
83	Third coaxial magnet	2.38(-5)	0.01	1.70
91	Mercury beam stop	6.04(-4)	0.34	1.07
92	Mercury beam stop	8.64(-4)	0.49	2.55
93	Mercury beam stop	1.13(-3)	0.64	4.01
94	Mercury beam stop	4.80(-4)	0.27	1.20
95	Mercury beam stop	4.42(-4)	0.25	1.57
96	Mercury beam stop	4.89(-4)	0.28	1.74
97	Mercury beam stop	5.34(-4)	0.30	1.89
98	Mercury beam stop	6.87(-4)	0.39	2.44
99	Mercury beam stop	6.61(-4)	0.37	2.35
100	Mercury beam stop	4.86(-4)	0.27	1.73
101	Mercury beam stop	3.65(-4)	0.21	0.93

operation at 1 MW with 24 GeV protons. To estimate the activation under different conditions, the results can be scaled by the number of MW-days.

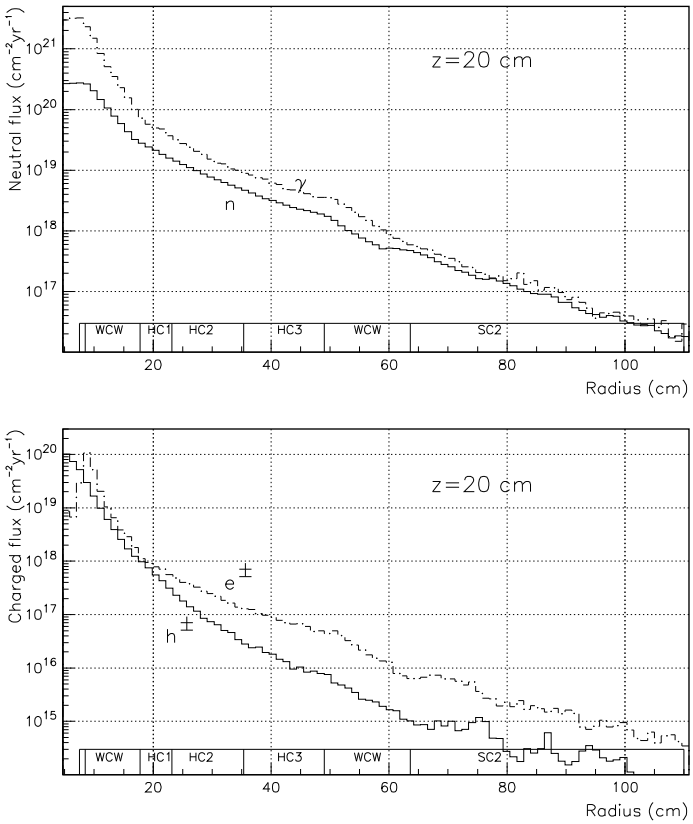

Figure 3.17: Flux of neutral (top) and charged (bottom) particles as a function of radius at the downstream end of the target.

Following operation of the machine for 100 days, the activity after 4 hrs, 1 day, 7 days, and 30 days of cooling has also been estimated. In addition, the total gamma-ray activity in each cell has been calculated, and used as input to a secondary calculation that determined the leakage of photons, and thus dose outside of the target module.

Tables 3.6-3.10 list the total neutron flux, activation, and gamma-ray intensity in various cells.

The values in Table 3.6 are the volume-averaged total neutron fluxes. The actual

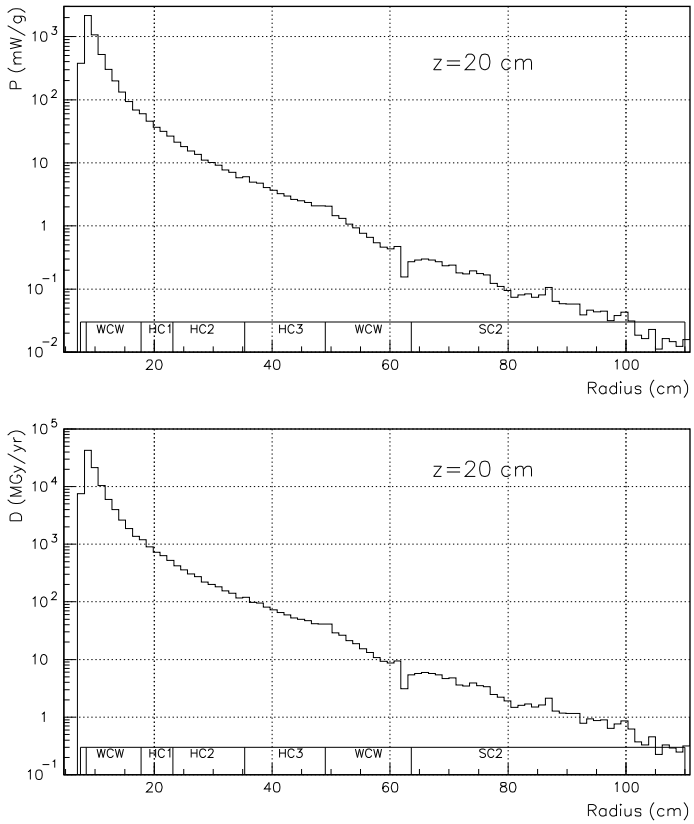

Figure 3.18: Power density (top) and total radiation dose (bottom) due to secondary particles as a function of radius at the downstream end of the target.

energy spectrum for each volume was used to determine the activation cross sections. Table 3.7 shows the resulting activation following 100 days of operation, and for selected time frames following machine shutdown.

The results in Table 3.7 are integral activation values for each of the cells. Each value is composed of contributions from hundreds of radioactive isotopes, which decay at different rates. Immediately following shutdown, the number of contributing isotopes is

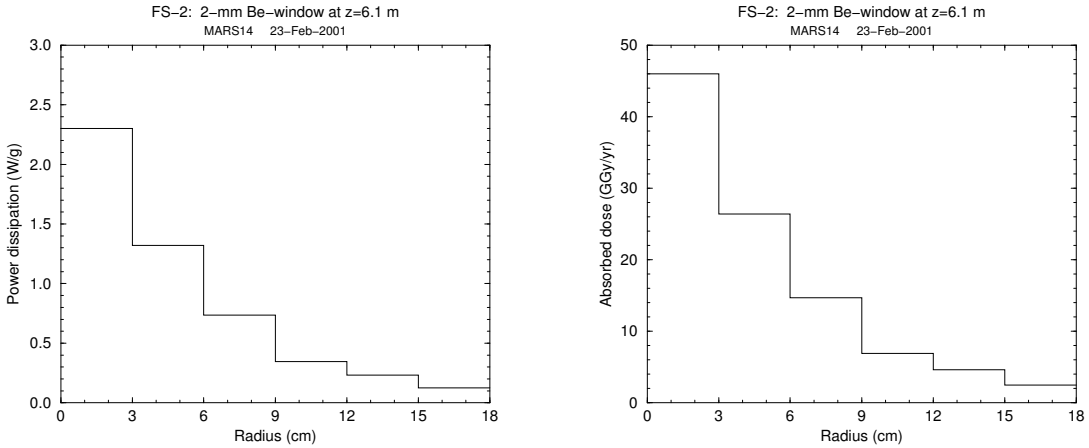

Figure 3.19: Power density (left) and absorbed radiation dose (right) in the beryllium window at $z = 6.1$ m.

extremely large. However, following 30 days of decay time, only the longest lived isotopes contribute, and generally there are only a limited number of isotopes at that stage. Two examples are presented in Tables 3.8 and 3.9, which list the major contributors to the activity after 30 days of decay time in a mercury pool cell (number 92), and a shield cell (number 8).

The major contributions to the activation of a mercury cell come from the isotopes closest to the target nucleus (mercury). The dominant contributor is an isotope of mercury, but there are significant contributions from lighter isotopes. Of particular interest are those that are, or could potentially be, volatile under operating conditions (Xe, Cs, Rb, *etc.*). Attention must also be paid to those elements that could pose material compatibility concerns when they come in contact with the structural materials of the cooling loop.

In the shield, the major contribution to the activation again comes from isotopes closest in mass to the target nucleus (primarily tungsten in this case). The distribution of major radioactive isotopes is different from the first case, although the tungsten and mercury nuclei are relatively close in mass. The reason for this difference is primarily due to the difference in proton energy of the spallating projectile particle and the fact that in the tungsten shield there is a significant amount of water present that softens the neutron spectrum. Finally, it should be noted that a significant amount of Be-7 (^{7}Be) is generated in this cell (all cells containing water will have Be-7 as part of their radioactive

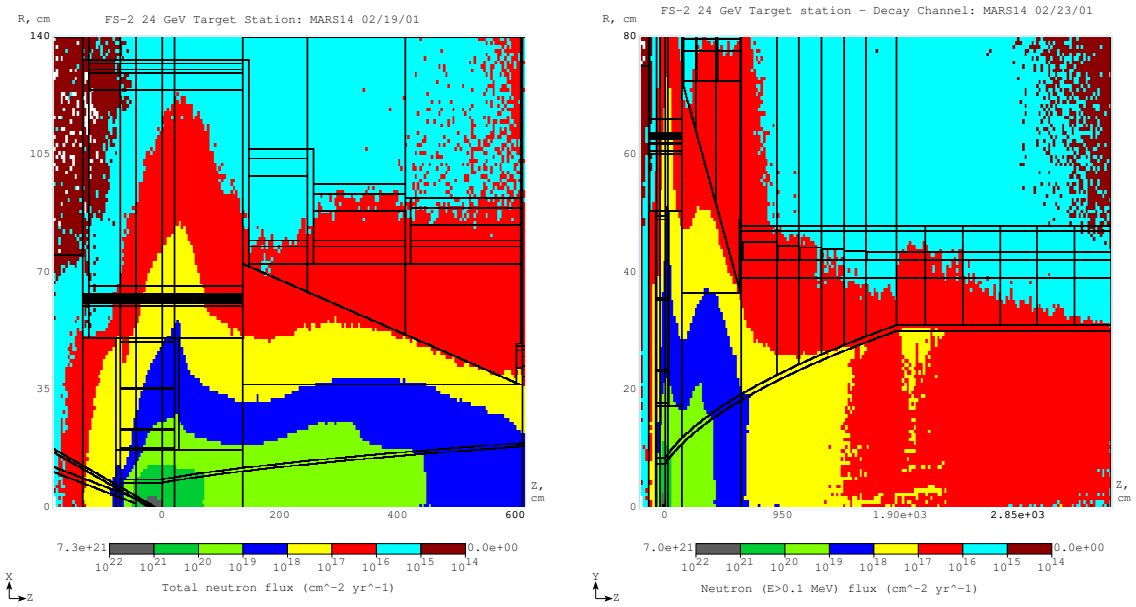

Figure 3.20: Flux of neutrons with $E > 100$ keV in the target system and decay channel for $-2 < z < 6$ m and $r < 1.4$ m (left) and $-2 < z < 36$ m (right) and $r < 0.8$ m.

inventory). This could be significant for operating the machine and maintaining the coolant loop. Tritium is also generated, and although it is not a major contributor to the overall inventory, its presence needs to be noted.

The radioactive nuclei considered here decay primarily by emitting a beta or gamma ray. These nuclides are generally not a personnel problem (unless they are ingested), since they are essentially totally self shielded by a component. However, the presence of gamma rays poses a personnel problem, and thus it is necessary to determine the gamma ray source strength associated with each of the above cells. This strength (as a function of gamma ray energy) can then be used in a separate calculation to determine the flux of gamma-rays leaving the target module, and the directional variation of the emitted radiation. The integrated source strength in photons per second for each volume as a function of time following shutdown is given in the Table 3.10.

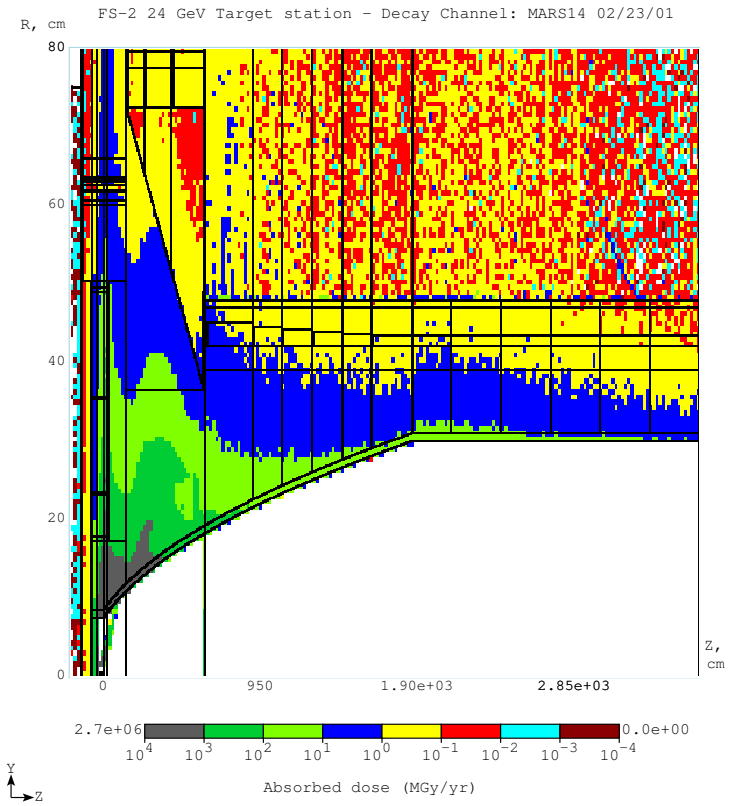

Figure 3.21: Absorbed radiation dose in the target system and decay channel for $-2 < z < 36$ m and $r < 0.8$ m.

3.3.3 Radial Leakage of Radiation from the Target Module

The mercury target is positioned in such a manner that it points downward at 100 mrad, and the proton beam points down at 67 mrad. Thus, the emerging shower of particles starts off in a downward direction. The charged particles are under the influence of the surrounding magnetic field, but the neutral particles propagate straight on. Any leakage flux from the target module will exhibit this overall pattern.

The results in Table 3.11 for radial leakage at the position of the mercury pool show the expected azimuthal variation, with more leakage in the direction of the proton beam. The gamma ray leakage is approximately an order of magnitude below that of the neutron leakage. The energy spectrum of the latter was also determined, and is given in Table 3.12.

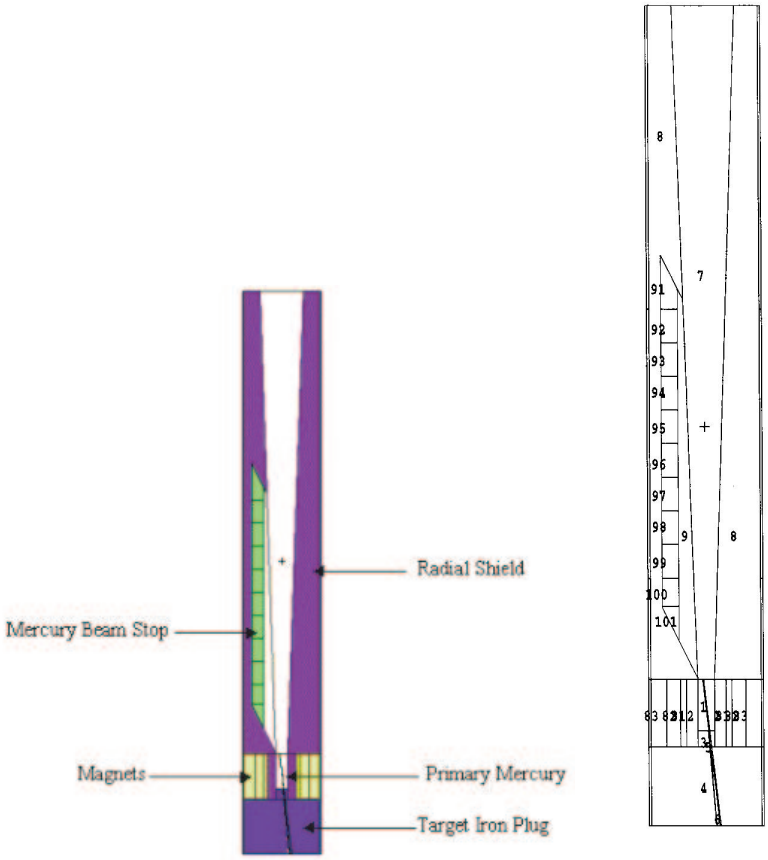

Figure 3.22: Longitudinal section through target module, with cell numbers shown on the right.

There is a significant neutron flux leakage above the MeV energy range, which will affect the operational life of components near the target magnet system.

3.4 Pion Capture Magnet

An efficient Neutrino Factory should capture nearly all the pions that the high-energy proton beam generates when it bombards the target. To do so, we employ a solenoidal magnetic field to bend the pion trajectories into helices bound to the surface of cylinders that enclose an invariant amount of flux. A solenoid captures those pions with trajec-

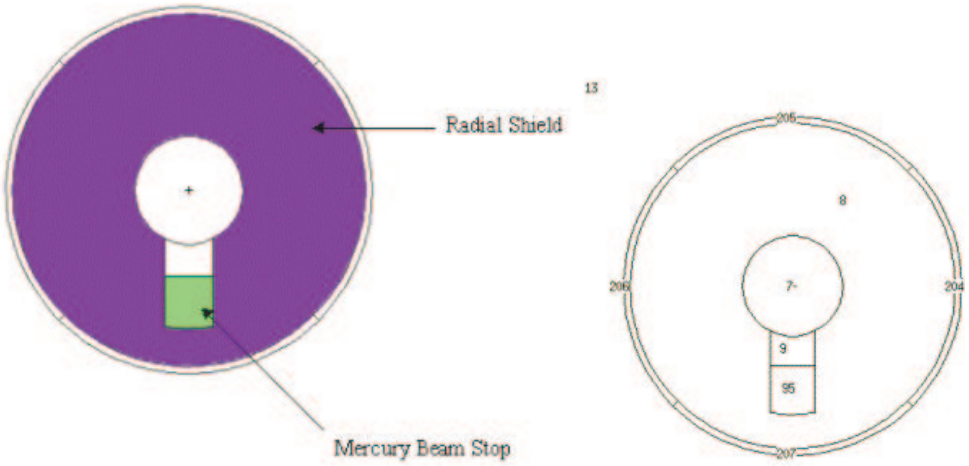

Figure 3.23: Radial section through the target module at $z = 4$ m, with cell numbers shown on the right.

tories small enough to fit inside its bore. Pions of high transverse momentum require a solenoid of large bore and intense field. For example, capture of transverse momenta up to 225 MeV/c, the baseline for Feasibility Study-II, requires a product of field and bore of 3 T·m. Study-II employs a capture field of 20 T, about the maximum that is feasible; the corresponding bore is 0.15 m.

The least costly magnet of this transverse-momentum reach has a large bore but only modest field. However, such a magnet would require that the magnets and other downstream components all be inconveniently large. Minimum overall system cost dictates a modest bore but high field.

The desired field profile of the pion capture magnet is uniform over the target, followed by a gradual transition to the much lower field of subsequent components of the Neutrino Factory, as shown in Fig. 3.8. For minimal particle loss the optimum field profile is

$$B(z) = \frac{B_0}{1 + kz/L}\,, \tag{3.2}$$

where B_0 is the field at $z = 0$, the downstream end of the target, and $(k + 1)$ is the ratio of B_0 to the field at $z = L$, the downstream end of the transition region. For Study-II, $B_0 = 19$ T, $k = 14.2$ and $L = 18$ m. Within the target region itself, $-l < z < 0$, where $l = 0.6$ m, the field need be only approximately uniform. Near the upstream end ($z = -l$) the drop in field should be at most 5%, in order to limit shearing of the incoming jet of

Table 3.6: Neutron flux in various target system cells for 1 MW of 24-GeV protons.

Cell Number	Total neutron flux ($cm^{-2}s^{-1} \times 10^{12}$)
8	1.27
12	8.64
2	8.02
3	9.32
81	3.27
82	1.29
83	0.26
91	4.07
92	3.51
93	3.12
94	2.88
95	3.28
96	4.63
97	6.43
98	8.98
99	10.06
100	7.56
101	6.49

mercury by the field gradient. Near the downstream end ($z = 0$) the field drops a similar amount in order to blend smoothly, satisfying $\nabla \cdot \mathbf{B} = 0$, with the rapid decrease with z of the field at the upstream end of the transition region.

To generate this field we employ magnets of three types: superconducting (SC), resistive, and iron. SC magnets generate the entire field everywhere except in the vicinity of the target. There, the intense field and high density of energy deposition from radiation make it more economical to supplement the SC magnet with a resistive one. Contributing to the field at the very upstream end of the target region is a stepped cylinder of ferromagnetic material. A cobalt-iron alloy such as Permendur could contribute nearly 1.2 T, but cobalt may be undesirable from the standpoint of activation. Pure iron would contribute slightly more than 1 T. More valuable than the modest and highly localized field contribution is the favorable field gradient, which corrects much of the field inhomogeneity of the other coils that would otherwise cause excessive shear of the jet of mercury

Table 3.7: Activation in Curies for selected cells. (x) stands for $\times 10^x$.

Cell	Time after shutdown				
Number	0	4 hrs	1 day	7 days	30 days
8	1.59(6)	2.63(5)	2.01(5)	1.37(5)	8.92(4)
12	7.67(3)	4.12(3)	2.58(3)	1.16(3)	5.45(2)
2	1.34(5)	2.11(4)	1.62(4)	1.11(4)	7.35(3)
3	6.26(2)	4.09(2)	2.95(2)	2.51(2)	1.87(2)
81	5.08(4)	3.32(4)	1.12(4)	2.12(2)	1.67(2)
82	7.85(4)	5.15(4)	1.74(4)	2.06(2)	1.59(2)
83	2.83(4)	1.85(4)	6.25(3)	8.53(1)	6.86(1)
91	1.24(3)	7.77(2)	5.08(2)	2.03(2)	8.93(1)
92	2.36(3)	1.46(3)	9.57(2)	3.87(2)	1.61(2)
93	2.44(3)	1.52(3)	9.99(2)	3.99(2)	1.62(2)
94	1.78(3)	1.15(3)	7.49(2)	2.99(2)	1.26(2)
95	1.75(3)	1.12(3)	7.41(2)	2.99(2)	1.25(2)
96	2.39(3)	1.52(3)	1.03(3)	4.05(2)	1.66(2)
97	2.78(3)	1.83(3)	1.24(3)	4.88(2)	1.99(2)
98	3.25(3)	2.15(3)	1.44(3)	5.40(2)	2.23(2)
99	2.98(3)	1.99(3)	1.35(3)	4.94(2)	1.96(2)
100	1.82(3)	1.25(3)	8.55(2)	3.00(2)	1.17(2)
101	9.93(2)	7.18(2)	5.04(2)	1.91(2)	7.55(1)

entering the target region.

Figure 3.24 shows the on-axis field profile of the proposed pion capture magnet with parameters $B_{\max} = 20$ T, $B_0 = B(-l) = 19.0$ T, $k = 14.2$, and $B(L) = 1.25$ T. Figure 3.25 sketches the magnets and cryostat for the region $-l < z < 6$ m. Tables 3.13 and 3.14 list the most important parameters of the hollow-conductor and first eight superconducting coils of the pion capture magnet.

Note that, Table 3.13 incorporates minor modifications to many of the coil parameters, that have not been taken into account in Table 3.2. For example, coils downstream of 6 m are shorter and more numerous; this is a consequence, of trying to maintain the field quality, in spite of the larger intercoil gaps, introduced to facilitate cryostat construction and installation.

Table 3.8: Activation for cell 92 (mercury) 30 days after shutdown. Only elements with more than one Curie are listed.

Isotope	Activation (Ci)	Isotope	Activation (Ci)
Hg-203	41.09	Lu-173	0.35
Au-196	0.87	Lu-172	1.19
Au-195	33.09	Lu-171	0.48
Pt-188	3.49	Yb-169	6.81
Ir-190	0.51	Cs-131	1.78
Ir-189	9.89	Xe-127	1.36
Ir-188	4.20	I-125	1.38
Os-185	10.71	Te-121	1.60
Re-183	7.99	Te-118	0.13
W-181	5.74	Sr-85	1.34
Ta-179	0.54	Rb-84	0.65
Ta-178	3.09	Rb-83	0.62
Hf-175	2.64		
Total 141.6 (Table 3.7 total 161.4)			

3.4.1 Hollow-Conductor Resistive Coils

In the baseline design of this Study, the resistive insert that surrounds the target region employs hollow conductors rather than a Bitter magnet, as was used in Feasibility Study-I [4]. The penalty in performance is significant, (see Section A.2.3), but this technology should survive much better in the harsh radiation environment around the target.

The hollow-conductor magnet also presents formidable engineering challenges. Radiation doses and neutron flux densities are very high. According to calculations using the MARS code [11], each operational year (taken for radiation estimates to be 2×10^7 s) adds a dosage of $\approx 10^9$ J/kg (10^9 grays, or 10^{11} rads) and a neutron flux of $\approx 2 \times 10^{19}/\mathrm{cm}^2$, despite ≈ 10 cm of shielding by water-cooled tungsten carbide that attenuates the neutron flux by more than an order of magnitude and the gamma dose by a factor of about 40. The intense ambient field, combined with the fairly large bore and fairly high current density, induces hoop stresses that are high compared with the low strength of typical hollow conductors, whose copper is in the annealed state for ease of processing. The neutron flux will strengthen the conductor to values associated with considerable cold work, but will also embrittle the conductor [15] so that the conductor must be supported

Table 3.9: Activation for cell 8 (tungsten-light water) 30 days after shutdown. Only elements with more than hundred Curies are listed.

Isotope	Activation (Ci)	Isotope	Activation (Ci)
Re-183	305.7	Gd-146	215.9
Re-184	171.6	Eu-149	276.5
W-181	40850.0	Eu-148	42.6
W-185	5779.0	Eu-147	256.9
W-178	9075.0	Eu-146	240.1
Ta-183	147.7	Eu-145	15.43
Ta-182	3122.0	Sm-145	115.2
Ta-179	3958.0	Pm-143	111.9
Ta-178	9077.0	Ce-139	174.0
Hf-175	5666.0	Cs-131	187.1
Hf-172	616.1	Xe-131	202.0
Lu-174	23.48	I-127	175.3
Lu-173	1104.0	Te-121	94.47
Lu-172	660.3	Te-118	9.849
Lu-171	576.6	Sn-113	101.3
Yb-169	2090.0	Ag-109m	47.96
Tm-170	9.611	Ag-105	190.1
Tm-168	27.28	Pd-103	105.4
Tm-167	274.0	Rh-103m	113.1
Dy-159	335.8	Rh-101	25.71
Gd-153	157.9	Rh-99	72.91
Gd-151	219.3	Be-7	1038.0
Gd-149	55.88	H-3	0.001
Total 88114.0 (Table 3.7 total 89210.0)			

as if it were glass. The alternative is to operate the conductor at 150°C or more (barely acceptable because of the penalty in conductor resistivity) or periodically to heat the conductor to that temperature, so as to anneal out much of the embrittlement before it becomes too severe.

The Study-II baseline design employs mineral insulated conductor (MIC) such as developed [16] for the Japan Hadron Facility. The insulation is a layer of MgO sandwiched between the conductor and its copper sheath. The conductor, shown in Fig. 3.26, is

Table 3.10: Gamma ray source (γ/s) in selected cells following machine shutdown. (x) stands for $\times 10^x$.

Cell	Time after shutdown			
Number	0	4 hrs.	1 day	30 days
8	1.31(17)	1.49(16)	9.76(15)	3.58(15)
12	1.01(15)	6.32(14)	2.98(14)	4.10(13)
2	1.11(16)	1.22(15)	8.13(14)	2.99(14)
3	4.35(13)	2.46(13)	1.44(13)	5.71(12)
81	1.54(15)	7.09(14)	2.43(14)	9.05(12)
82	2.26(15)	1.09(15)	3.71(14)	8.58(12)
83	8.26(14)	3.44(14)	1.34(14)	3.74(12)
91	2.05(14)	1.44(14)	6.49(13)	7.39(12)
92	2.95(14)	1.99(14)	1.07(14)	1.52(13)
93	4.29(14)	3.08(14)	1.39(14)	1.55(13)
94	3.02(14)	2.21(14)	1.03(14)	1.23(13)
95	2.45(14)	1.71(14)	8.85(13)	1.19(13)
96	3.48(14)	2.45(14)	1.23(14)	1.54(13)
97	4.36(14)	3.14(14)	1.57(14)	1.99(13)
98	5.10(14)	3.88(14)	1.89(14)	2.28(13)
99	4.86(14)	3.66(14)	1.69(14)	1.80(13)
100	2.86(14)	2.17(14)	1.02(14)	1.01(13)
101	1.47(14)	1.16(14)	5.49(13)	5.86(12)

Table 3.11: Integrated neutron and gamma ray flux per proton leaking radially outward from the target system at $z = 4$ m, the location of the mercury pool.

Cell Number	Neutron flux ($\mathrm{cm^{-2}s^{-1}} \times 10^{-4}$)	Gamma ray flux ($\mathrm{cm^{-2}s^{-1}} \times 10^{-5}$)
204	1.72	4.10
205	1.29	3.14
206	1.69	4.24
207	3.94	1.11

Table 3.12: Neutron energy spectrum for cell 207, the cell below the mercury pool. (x) stands for $\times 10^x$.

Energy bin (MeV)	Flux
0.0- 0.01	6.40(-5)
0.1- 0.1	6.01(-5)
0.1 - 1.0	1.31(-4)
1.0- 5.0	5.89(-5)
5.0 - 10.0	1.49(-5)
10.0 - 100.0	5.05(-5)
100.0 - 1000.0	1.37(-5)
1000.0 - 24000.0	2.237(-8)
Total	3.936(-4)

Table 3.13: Parameters of the hollow-conductor magnets.

	H-C 1	H-C 2	H-C 3
Avg. current density (A/mm^2)	244	191	149
Winding inner radius (cm)	17.8	23.2	35.3
Winding outer radius (cm)	23.2	35.3	49.0
Radial build of windings (cm)	5.4	12.2	13.7
Upstream end, z_1 (cm)	-71.2	-71.2	-71.2
Downstream end, z_2 (cm)	3.7	16.5	36.1
Coil length, $z_2 - z_1$ (cm)	74.9	87.7	107.3
Volume of windings (m^3)	0.052	0.196	0.389
Approx. peak field (T)	20.0	18.6	16.1
Avg. hoop tension (MPa)	118	124	115
Conductor fraction (%)	33.2	32.9	33.4
Copper fraction (%)	48.9	48.3	49.2
Structural fraction (%)	11.2	12.1	10.7
Copper mass (tons)	0.243	0.893	1.77
Stainless steel mass (tons)	0.048	0.194	0.334

18 mm square, with a cooling hole that is 10 mm square, surrounded by insulation 1.8 mm thick and a copper sheath 1.1 mm thick, for an overall size of 23.8 mm. As employed

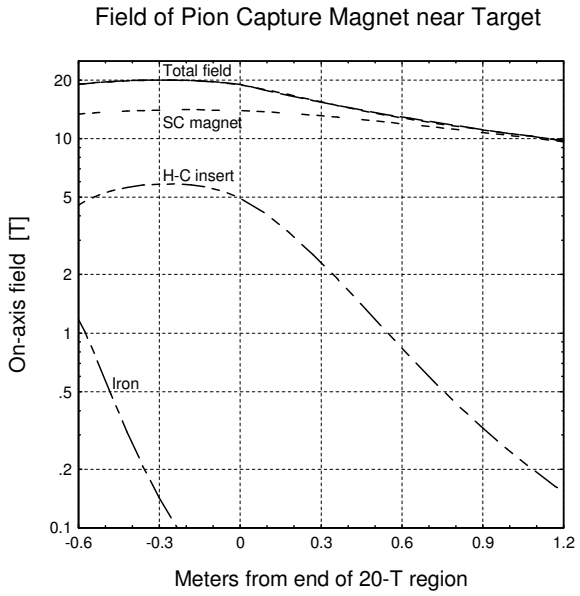

Figure 3.24: On-axis field of the pion capture magnet near the target region, $-0.6 < z < 1.2$ m. At $z = -0.3$ m, the superconducting magnet generates about 14 T and the resistive insert 6 T. The iron improves the entry of the mercury jet into the region by reducing the field inhomogeneity by a factor of two.

by the JHF, in lengths of 60 m and with only modest water pressure, the conductor can carry 3 kA. By limiting each hydraulic length to 15 m and using a high water pressure differential, 30 atm, as used at the National High Magnetic Field Laboratory (NHMFL), such a conductor will carry the required current, 15.5 kA, with a bulk temperature rise limited to 60°C. With an inlet water temperature of 10°C, as at the NHMFL, the peak conductor temperature is 80°C.

Figure 3.27 shows the cross section and a longitudinal section of the resistive insert magnet, built from three grades of such hollow conductor. The magnet consists of three nested coils, the innermost of two layers and the outer two coils of four layers each. Surrounding each coil is a reinforcing cylinder of Inconel 718, maraging steel, or other high-strength material. These cylinders hold the downstream flange against the downstream load of ≈ 0.6 MN (60 metric tons) from the other magnets in the system. Simultaneously, the cylinders contain the conductor against the high Lorentz forces. To restrict all terminations to the upstream end, the conductor spirals to the downstream

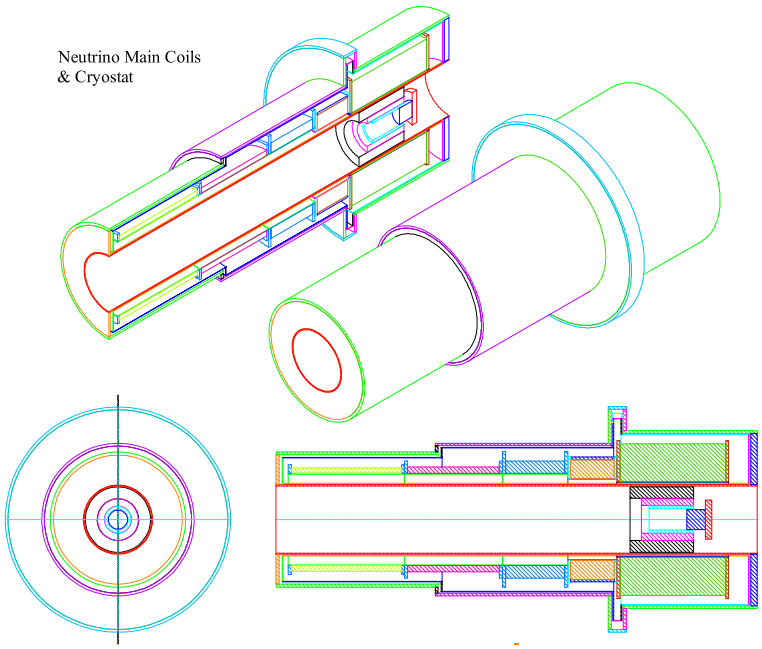

Figure 3.25: Cryostat and coils of the pion capture magnet in the region $-1 < z < 6$ m. The proton beam enters from the right of the section view in the lower right of the figure. Shown: iron plug (of stepped, T cross section), hollow-conductor (H-C) insert magnet, tungsten shielding outside H-C insert, cryostat, and first five superconducting (SC) coils. The bores of the SC coils range from 1.27 to 1.55 m. The first SC coil generates 14 T; the field at the downstream end of the fifth coil is 3.3 T. Not shown: conical beam tube and shielding between it and cryostat. Further downstream are additional SC coils to extend the field tail to 1.25 T at $z = 18$ m.

end in odd-numbered layers and back in even-numbered layers. To achieve water flow adequate to limit the bulk temperature rise to 60°C with conductors within the capacity of the JHF drawing bench, all layers have six conductors hydraulically in parallel, *i.e.*, a six-in-hand winding. That is, all conductors are electrically in series and hydraulically in parallel.

The inner coil uses conductor exactly as shown in Fig. 3.26. The other coils use conductor of the same proportions, to permit fabrication from billets of the same dimensions

Table 3.14: Parameters of the upstream eight superconducting solenoids of the pion capture system.

	SC 1	SC 2	SC 3	SC 4	SC 5	SC 6	SC 7	SC 8
Avg. current density (A/mm^2)	234	255	297	383	484	679	705	705
Winding inner radius (cm)	63.6	68.6	77.6	77.6	77.6	42.4	42.2	42.2
Winding outer radius (cm)	127.8	101.1	98.8	88.3	84.1	45.1	45.9	45.9
Radial build of windings (cm)	64.2	32.5	21.2	10.7	6.56	2.69	3.69	3.69
Upstream end, z_1 (cm)	-125.3	62.8	145.7	255.6	420.6	600.8	657.7	720.7
Downstream end, z_2 (cm)	52.8	135.7	245.6	410.6	606.5	643.7	707.3	770.3
Coil length, $z_2 - z_1$ (cm)	178.1	72.9	99.9	155.0	185.9	42.9	49.6	49.6
Volume of windings (m^3)	6.88	1.26	1.17	0.866	0.619	0.032	0.051	0.051
Approx. peak field (T)	14.0	11.8	8.74	6.21	4.33	3.33	3.03	3.03
Avg. hoop tension (MPa)	209	206	201	184	163	96	90	90
Conductor fraction (%)	7.8	6.2	5.3	5.5	6.2	8.2	8.3	8.3
Copper fraction (%)	10.4	10.9	12.1	16.4	21.8	38.5	39.9	39.9
Structural fraction (%)	31.8	32.9	32.6	28	22	3.4	1.8	1.8
Vol. of superconductor (liters)	538	79	62	48	38	3	4	4
Copper mass (tons)	6.42	1.24	1.28	1.27	1.21	0.11	0.18	0.18
Stainless steel mass (tons)	17.1	3.24	2.98	1.89	1.06	0.01	0.01	0.01

as that for the inner coil. These outer coils, being longer as well as larger in diameter, have longer passages that require bigger conductor, 26.8 mm for the coil of intermediate size and 30.6 mm for the outer coil. Each conductor in the outermost double layer is 35 m long, with a mass equivalent to 57 m of 23.8 mm square conductor. This is within 5% of the maximum so far produced on the JHF drawing bench, and thus sets the limit on conductor size throughout the magnet.

3.4.2 Superconducting Coils

One of the superconducting coils of the pion capture magnet is also a formidable engineering challenge: SC 1, with its 14-T field and 1.3-m bore. Fortunately there are two precedents for this coil. One, is a collaboration of MIT and the NHMFL for its 45-T hybrid magnet [17]. It can generate 15 T when operated alone, and therefore not restricted to 14 T by the need for current margin to survive the current surge from a tripout or burnout of the insert coil of the hybrid system. However, the bore of this magnet is only half that of pion capture magnet SC 1. More relevant is the central solenoid model coil

Figure 3.26: Mineral-insulated hollow conductor developed for Japan Hadron Facility. The end-on view shows the white layer of powdered MgO insulation sandwiched between the copper hollow conductor and its sheath, also of copper. Of the cross section, 17% is cooling passage, 37% conductor, 28% insulation and 18% sheath. The side view shows a conductor termination, brazed of several parts that confine the MgO and hold the glossy white ceramic ring that keeps the sheath isolated from the current-carrying conductor.

(CSMC), shown in Fig. 3.28, for ITER, the International Thermonuclear Experimental Reactor [18]. The coil has generated 13 T in a bore 26% bigger than necessary for SC 1. The CSMC weighs 140 tons and stores 600 MJ, the same as the entire pion capture magnet, including the coils in its 18-m-long transition region.

The pion capture magnet has the additional complexity of energy deposition from radiation, up to 1 kW/m^3, despite shielding about 30 cm thick. However, it does not have to cope with energy deposition from the high sweep rate that the CSMC must survive. It also does not have to cope with so high a discharge voltage, 15 kV for the CSMC. Therefore, its insulation need not be so thick, nor its current density quite so low.

Cable-in-conduit conductor (CICC) will be used in the highest field superconducting coils of the pion capture magnet, coils SC 1–5. Figures 3.29 and 3.30 show the CSMC conductor, which is about 50 mm square and can carry 46 kA in a field of over 13 T. Liquid helium in the central tube flows through the spiral gap in its wall to cool the strands

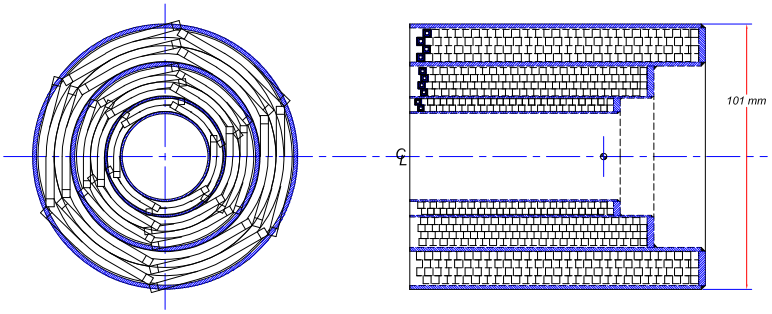

Figure 3.27: End view (left) and vertical section (right) of the resistive insert of the hollow-conductor magnet. Every layer employs six hydraulic paths in parallel to achieve the short hydraulic path length necessary for adequate water flow. The conductor is mineral-insulated conductor (MIC) of the sort developed for the Japan Hadron Facility, shown in Fig. 3.26. The thick-walled cylinders reinforce the conductor against the radial Lorentz hoop stresses engendered by the combination of high field (20 T) and large bore (0.36 m).

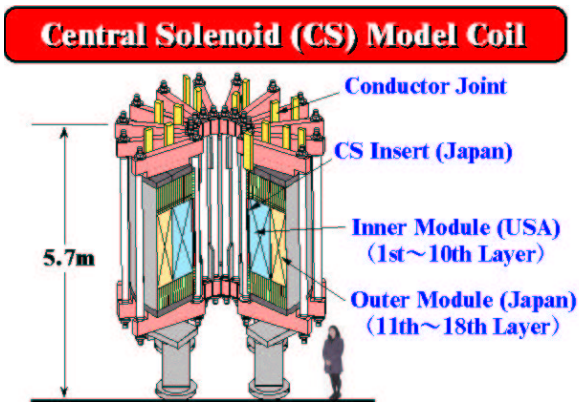

Figure 3.28: Superconducting magnet of the same scale as the pion capture magnet. The CSMC for ITER weighs 100 tons, generates 13 T in a 1.6 m bore, and stores 600 MJ.

of superconducting cable that parallel the tube. The fine strands have a high ratio of surface to volume, to keep each strand at nearly the same temperature as the helium.

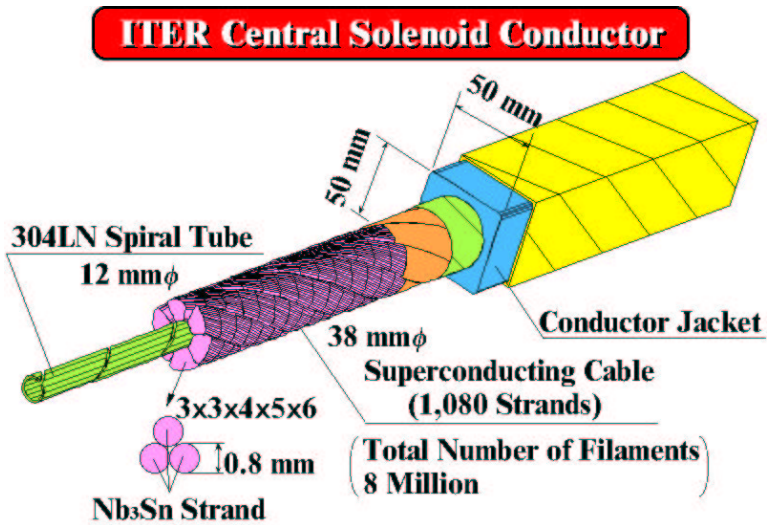

Figure 3.29: Concept of high-current cable-in-conduit conductor needed by the intense-field coils of the pion capture magnet. Liquid helium in the central tube flows through the spiral gap in its wall to cool the strands of superconducting cable that parallel the central tube. The outer jacket, typically of stainless steel or Inconel, provides most of the mechanical strength.

The outer jacket, typically of stainless steel or Inconel 908, protects the delicate strands within and provides almost all of the mechanical strength to resist huge Lorentz forces in large magnets that generate intense fields. Cable-in-conduit conductor is appropriate for large magnets operating at 10 kA or more. For the downstream coils of the pion capture magnet, which experience lower hoop and much lower axial loads, solid conductors or Rutherford cables are simpler and more economical.

3.4.3 Magnetic Forces

The axial loads on the upstream, high-field coils of the pion capture magnet are immense. Figure 3.31 shows that the peak cumulative axial load (which is at the downstream end of SC 1) to be over 100 MN, or 10,000 metric tons. All of the biggest loads involve only the first five SC coils. To manage this load, we support the coils with a structure that is cold at both ends to minimize heat leaks into the cryostat. The obvious way to do this is to house them all in the same cryostat. This is the only feasible way given that the

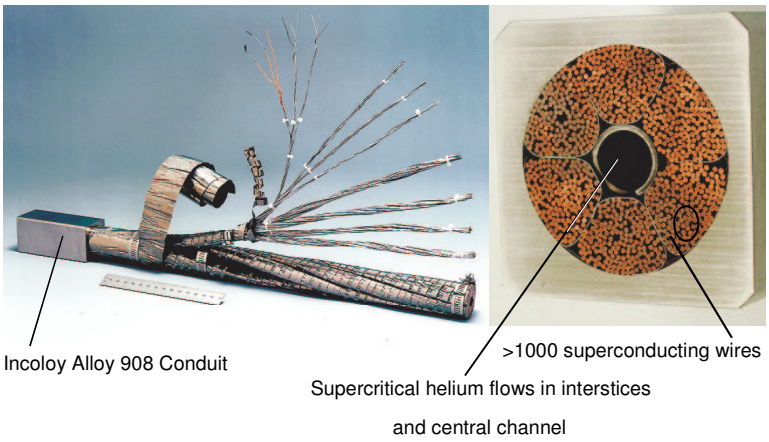

Figure 3.30: The cable-in-conduit conductor for the ITER central solenoid.

separation between consecutive coils is 10 cm, which is not enough for two sets of coil flanges and cryostat walls. The loads on all the low-field coils (beyond $z = 6$ m) sum to only 2.5 MN. We group these coils in sets, as in the case of phase rotation coils, with each cryostat of convenient length.

3.4.4 Field Quality

The gaps between consecutive coils can introduce considerable field ripple, especially beyond $z = 6$ m, the downstream end of the proton beam absorber, where the coils are of smaller bore. Fig. 3.32 shows the field ripple for coils with 14 cm gaps as indicated in Table 3.14. Whereas Table 3.2 had only 7 coils downstream of $z = 6$ m, Table 3.14 has 19 coils, each of only ≈ 50 cm in length. This geometric distribution maintains the field ripple within 5.3% peak-to-peak and 10% rms. An on-axis field ripple of this size does not affect the transmission of pions to the phase rotation region.

3.5 Beam Windows

3.5.1 Upstream Proton Beam Window

The upstream and downstream beam windows isolate the incoming proton beam transport and pion decay channel from the mercury vapor atmosphere near the target.

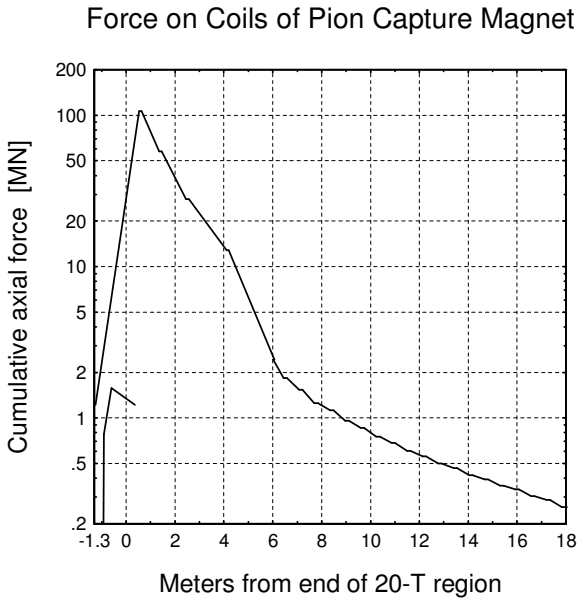

Figure 3.31: Cumulative axial force on components of the pion capture magnet. Upper curve: the peak force is over 100 MN, or about 10,000 metric tons. The forces between the first five superconducting coils, with their high field and large size, dictate that they share a common cryostat. The forces on coils beyond $z = 6$ m are much less, and allow individual cryostats for each coil or convenient group of coils. Lower curve: the force on the resistive insert magnet and iron is only 1.2 MN (note the semi-logarithmic scale).

The upstream proton beam window will see the full beam before it hits the target. The resulting pulsed energy deposition excites pressure waves that must be sustained by the window for over 10^8 cycles per year. Since the lifetime of the window is expected to be limited, provisions for its periodic replacement are part of its design.

The proton beam window is a double wall structure with a gap between the two walls that allows for active cooling. The interior face of the window will be exposed to mercury vapor, so the window material must be mercury compatible. Candidate window materials include beryllium and Ti90-Al6-V4 alloy (whose short-term compatibility with mercury has recently been verified).

To assess the viability of candidate window materials, an ANSYS finite-element analysis was performed, including both the thermal aspect of the beam/window interaction

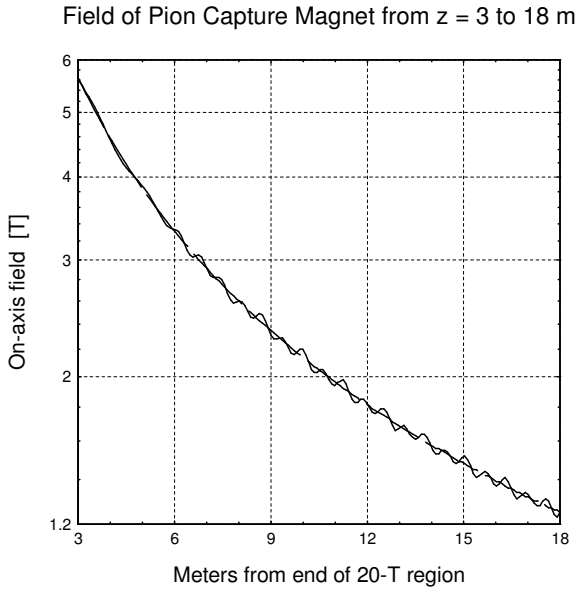

Figure 3.32: On-axis field of the pion capture magnet from 3 to 18 m downstream of the target region, where the solenoids have 0.42 m inner radius and 0.50 m length separated by axial gaps 0.14 m. The desired field (dashed line), to maximize the adiabatic retention of captured pions, declines from 19 T at $z = 0$ to 1.25 T at 18 m according to Eq. 3.2. The actual field (solid line) differs from the desired value by 5.3% peak-to-peak (from -2.5% to $+2.8\%$), with an rms deviation of 1.0% (Note the semi-logarithmic scale).

and the resulting thermal shock. The energy deposition in the window material was computed using the MARS code [10]–[11]. Figure 3.33 shows results for a 1-mm-thick beryllium window intercepting six pulses of 1.7×10^{13} 24-GeV protons with $\sigma_r = 1$ mm. Figure 3.33 (left) shows the temperature rise of one of the walls of the beryllium window during a train of six micro-pulses that arrive 20 ms apart. Bunches of these six micropulses arrive at a frequency of 2.5 Hz. The temperature rise per micro-pulse, at the center of the beam, is approximately 10°C. In steady-state conditions, coolant flowing between the walls, would limit the temperature in the window to ≈ 116°C above ambient, assuming a heat removal coefficient of 100 W/m$^2 \cdot$°C.

Figure 3.33 (right) shows the von Mises stress induced in the Be window by a single micropulse. The peak stress is about 90 MPa while the yield strength of beryllium is

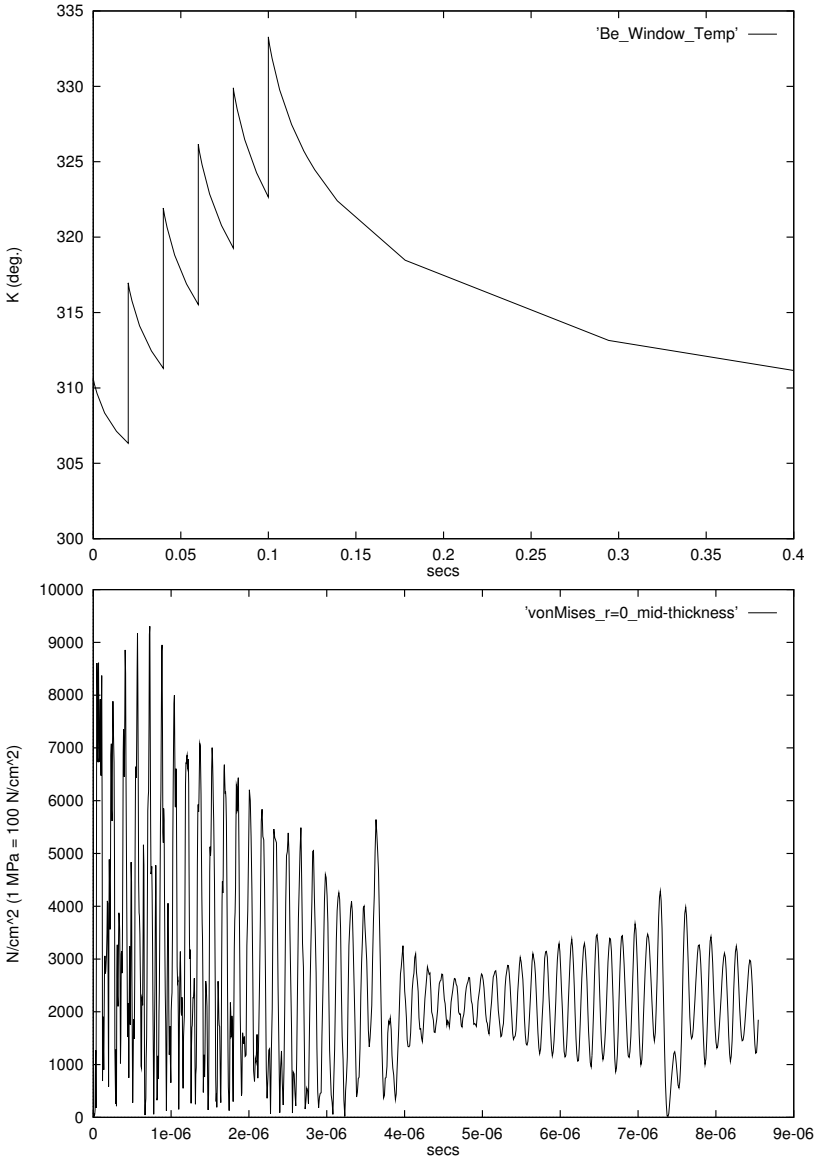

Figure 3.33: ANSYS model of a 1-mm-thick beryllium window subject to a train of six micro-pulses of 1.7×10^{13} 24-GeV protons per pulse with $\sigma_r =$ 1 mm). Top: transient thermal response; bottom: von Mises stress.

between 186 and 262 MPa. We note that the beam spot on the window will certainly be larger than that assumed here. The spot size at the window is related to that at the

target by

$$\sigma_{r,\text{window}} = \sigma_{r,\text{target}} \sqrt{1 + \frac{L^2_{\text{window}}}{\beta^{\star 2}}}, \tag{3.3}$$

where, $\sigma_{\text{target}} = 1.5$ mm, L_{window} is the distance from the window to the target, and $\beta^\star$ is the betatron parameter of the beam focus (not yet determined). Clearly, large L and small $\beta^\star$ provide greater safety margin for the beam. In the present design, $L_{\text{window}} \approx 3.3$ m, but parameters of the proton beam focus, including $\beta^\star$, have not been set. In any case, we have taken a very conservative estimate of the spot size, so we have a significant safety margin.

3.5.2 Downstream Beam Window

The downstream beam window is located on the magnetic axis at $z = 6$ m and will be approximately 36 cm in diameter. It intercepts forward secondary particles, but not the unscattered proton beam. The baseline window design is a pair of 2-mm-thick Be plates with active cooling between them.

A MARS calculation of the power deposition and radiation dose in the Be window is shown in Fig. 3.19. The dose is high enough that the Be window is not a lifetime component. A preliminary concept for window replacement is shown in Fig. 3.39.

The mechanical design of the downstream window is governed by the following:

- Large window diameter (36 cm)
- Pressurized active coolant in the gap of the double wall
- Vacuum environment on the downstream side

The principal design challenge is to maintain mechanical integrity against the pressure differential over the large window area. Failure due to beam-induced stress is a lesser concern for this window.

Three variations of the basic design concept are being considered, as shown in Fig. 3.34. For a window with flat plates, as in Fig. 3.34 c), the stress at the edge of the plates due to a one atmosphere pressure differential is above the yield strength. To relieve the stress the windows should be curved, as in Fig. 3.34 a) and b). Option a) in which the two windows have equal but opposite curvature, appears to be more favorable, with a steady-state temperature gradient of only 30°C. If no coolant were used, the temperature gradient would be 250°C.

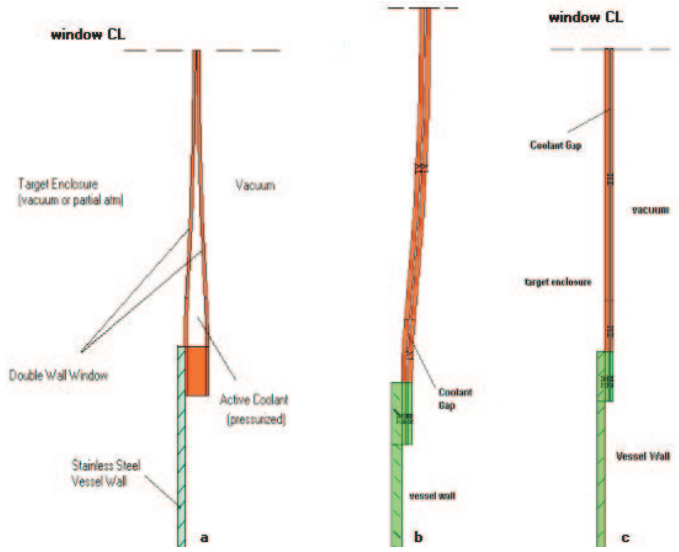

Figure 3.34: Three double layer designs for the downstream beam window.

3.6 Mercury Deflectors

Two components of the mercury handling system present unusual design challenges in view of the disruptive effect of the proton-mercury interaction: i) the mercury jet nozzle and ii) the entrance baffles to the mercury pool that serves as the proton beam absorber.

3.6.1 Mercury Jet Nozzle

Pressure waves generated in the mercury jet during its interaction with the proton beam will travel back to the nozzle, which must withstand the pressure wave. An ANSYS model of the effect of a pulse of 1.7×10^{13} 24-GeV protons on a 5-mm-radius mercury jet indicates a peak stress of 3800 MPa. The resulting pressure wave propagates to the nozzle in about 100 μs where the pressure pulse will be about 100 MPa, as shown in Fig. 3.35.

The nozzle must be constructed of a material with yield strength well above 100 MPa to have the desired lifetime of $> 10^8$ cycles.

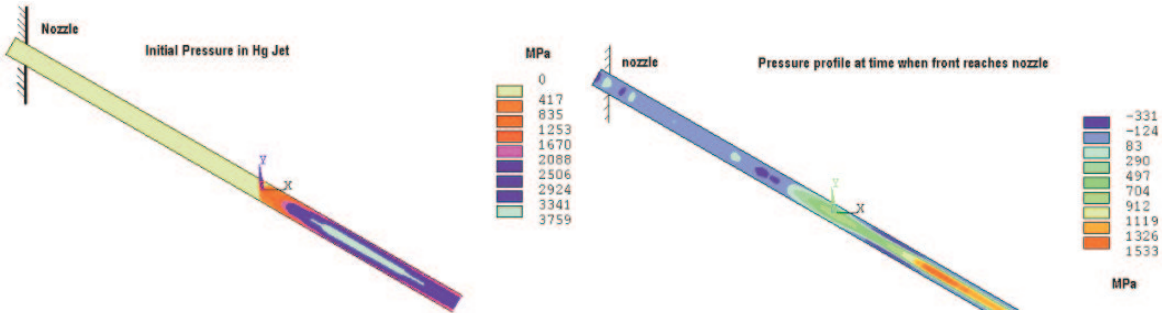

Figure 3.35: ANSYS model of the pressure wave in the mercury jet induced by a pulse of 1.7×10^{13} 24-GeV protons. Left: the pressure profile just after the proton pulse; right: the pressure profile when the wave reaches the nozzle after 100 μs.

3.6.2 Entrance Baffles to the Mercury Pool

Both the unscattered proton beam and the undisrupted mercury jet enter a pool of mercury at $2.25 < z < 5$ that serves as the proton beam absorber. Details of this concept are shown in Fig. 3.36.

The undisrupted mercury jet has mechanical power $\pi\rho r^2 v^3/2 \approx 10$ kW for $r = 5$ mm and $v = 30$ m/s. This power will agitate the mercury pool unless the impact of the jet is mitigated by a set of diffusers submerged in the pool. The diffusers will consist of stainless steel mesh and a bed of tungsten balls.

The unscattered part of the proton beam retains about 10% of the initial beam power, which is sufficient to disperse a significant volume of mercury as it enters the pool. A set of stainless-steel-mesh baffles will direct the ejected mercury droplets back into the pool. The design must be robust enough to survive at least one pulse in which the mercury jet was not present and the full proton beam entered the pool.

3.7 Mercury Flow Loop

The mercury-jet target system consists of the process flow loop, a replaceable nozzle assembly mounted in the bore of the iron plug magnet, a mercury containment vessel that is part of the decay channel downstream to $z = 6.1$ m, and the beam absorber, which is located at $2.5 < z < 5.5$ m. A dedicated hot cell that contains the flow loop components is located at the tunnel level. Figure 3.37 is a schematic diagram of the

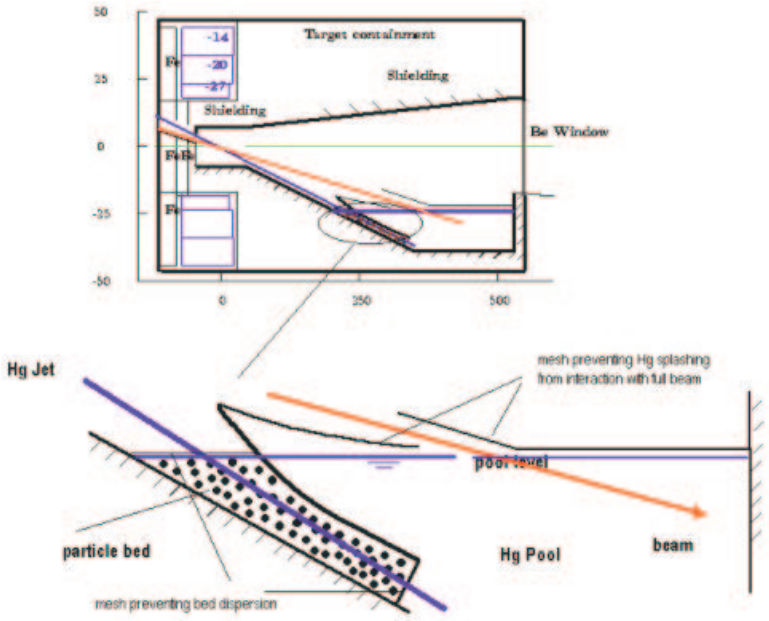

Figure 3.36: Schematic of the mercury pool that serves as the proton beam absorber.

overall system.

3.7.1 Process Flow Loop and Absorber

The process flow loop contains 110 liters of mercury distributed as follows: 30 liters in the beam absorber pool, 7 liters in the heat exchanger, 35 liters in the sump tank, and 38 liters in miscellaneous piping and valves. A 200 liters tank provides storage for the mercury when the system is shut down or undergoing maintenance. The piping is sloped towards the storage tank, and the elevation of the main (jet) pump, the heat exchanger, the beam absorber pool, and the storage tank are arranged so that the mercury level can be easily controlled among the components. Various valves are used to isolate portions of the system for storage, flow, or drainage into the storage tank, and drainage is by means of gravity. The system components are located in the target hot cell and are arranged to be accessible by the wall-mounted manipulators. The various valves are pneumatically actuated, but they can be manually operated using through-the-wall manipulators, if necessary.

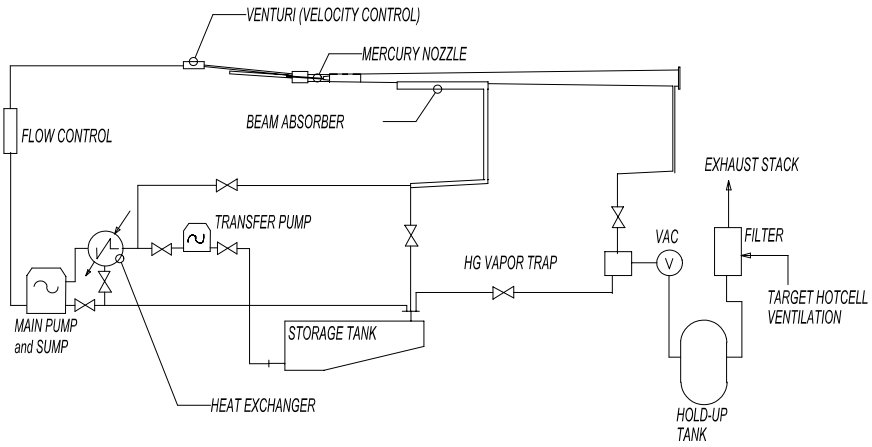

Figure 3.37: Mercury flow loop schematic layout.

The pumps for the flow loop have centrifugal magnetic drives. The low-capacity transfer pump is self-priming and can pump at a rate of 3-6 gpm. This pump is used to transfer mercury from the storage tank into the flow loop by first filling the heat exchanger and the sump tank of the main pump. The volume of the sump tank includes Hg for the absorber pool as well as the main pump volume, *i.e.*, 65 liters. The high-capacity main pump initially transfers 30 liters of mercury into the pool before the high-field magnets

are energized. During system operation, it pumps at a rate of 35–50 gpm to circulate mercury at 30 m/s through the nozzle assembly.

The heat exchanger is a welded-tube and shell construction with a closed-loop water system. The inlet temperature of the mercury is 122°C; the outlet temperature is 20°C. The water inlet temperature is 20°C; the outlet temperature is 47°C. These values are based on water flowing through the shell of the exchanger at 4 liters/s. Figure 3.38 is a view of the flow loop components located in the target hot cell.

The mercury storage tank is located under the shield floor in the target hot cell. The full inventory of mercury is stored there when the system is shut down. This is accomplished by closing and opening the appropriate valves in the flow loop for gravity flow into the tank. There are drain lines from the sump pump, the heat exchanger, and the beam absorber pool. In addition, there is a secondary drain/vent located at $z = 6.0$ m. Its purpose is to extract and condense mercury vapors prior to maintenance operations that require opening the mercury containment vessel in the capture/decay region. The vent line is connected in series to a mercury trap (condenser) and a vacuum scroll pump. The condensate is returned to the storage tank by means of a bypass line and the vacuum exhaust passes into the first hold-up tank. Gases and mercury vapors are passed through a filter system containing sulfur-treated charcoal filter modules before passing into the facility ventilation exhaust.

Mercury, mercury vapor, and rare gas reaction products are contained in the target/capture region by means of windows. The upstream Be window is mounted on the target nozzle insert at the proton beam line axis; the downstream beryllium window is mounted to the vacuum vessel at SC 6. Figure 3.39 shows the location of the beryllium window.

The average beam power deposited in the jet is 400 W/g (100 kW) and the remainder of the 1-MW proton beam power is deposited in the shielding that lines the target magnet system, including the mercury pool that serves as the proton beam absorber. Even if 900 kW were deposited in the beam absorber, the bulk temperature rise of mercury in the absorber pool would be only 102°C, well below the boiling point. However, this assumes homogeneous mixing occurs in the pool due to the mercury jet that enters the pool at a rate of 2.4 liters/s.

3.7.2 Target System Maintenance

The various components that make up the target system fall into three categories. Class 1 are limited-lifetime components that require frequently scheduled remote replacements during the life of the facility. They are designed for remote handling and minimal impact

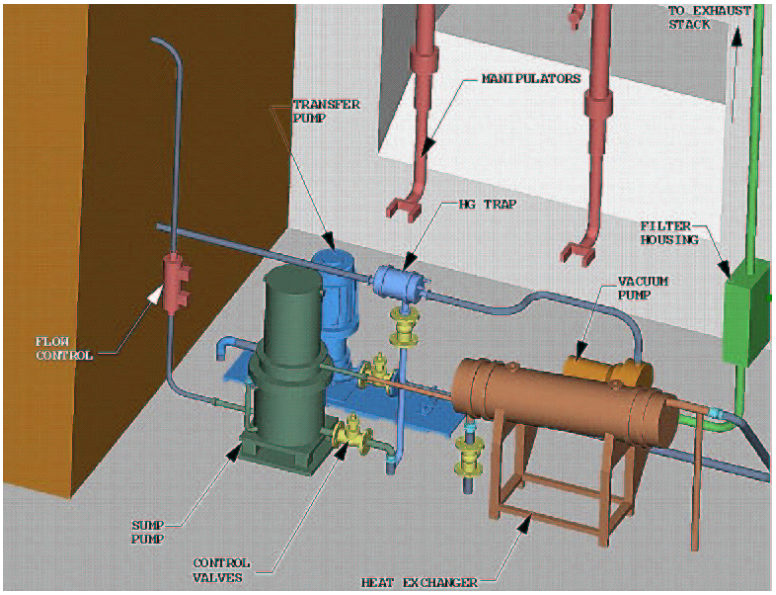

Figure 3.38: Arrangement of the mercury flow loop components in the target hot cell.

on operating availability, and remote handling tools and equipment are included in the design. Class 2 are lifetime components having activation levels that preclude hands-on replacement, and whose failure shuts down the facility. They have a finite probability of at least one failure. These components are designed for remote handling, but remote handling tools and equipment are not included in the design (unless they are used for initial installation). Their replacement would impact operating availability since spare components are not assumed to be on hand. Class 3 components are expected not to fail during the facility lifetime.

Replacement of target system components must be done using remote-handling equipment because of high levels of activation, and the presence of (radioactive) mercury contamination. The target system contains many components that are considered to be life-of-the-facility (Class 3), numerous components that could require infrequent replacement (Class 2), and several that are life limited (Class 1). The maintenance requirements for this system are summarized in Table 3.15. The table is based on an operating year of 2×10^7 seconds, which is the equivalent of 8 months of continuous full-intensity beamline operation.

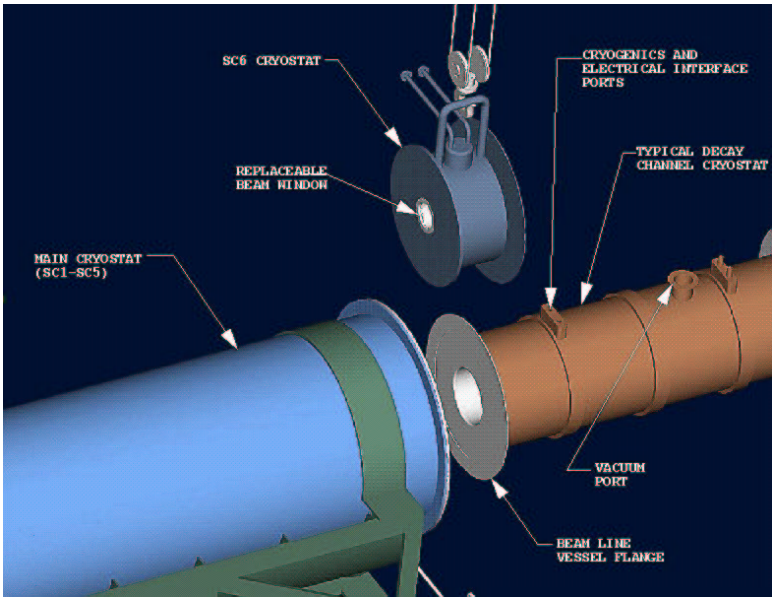

Figure 3.39: The beryllium window is mounted to a readily replaceable solenoid.

Table 3.15: Maintenance requirements for the target system components, based on 8-hour maintenance shifts.

Component	Class	Failure Mode	Dose Rate (rad/h)	Expected Life (yrs)	Replacement Time (days)
Nozzle insert	1	erosion, embrittlement	$> 10^6$	2–3	11–16
Be window	1	embrittlement	10^4–10^5	2	7–11
Isolation valve	1	mechanical	10^4–10^5	5–7	1–2
Filters	1	saturated	Contam.	2	2–3
Pumps, valves	2	mechanical	Contam.	7.5	2–3
Heat exchanger, Piping, tanks	3	mechanical	Contam.	> 40	5–8

3.8 Target Support Facility

The geometry for the target support facility (see Fig. 3.12) is defined around the intersection of the mercury jet, the proton beam, and the magnetic axis of the solenoid

magnets. The proton beam interacts with the jet over a region whose downstream end is at $z = 0$ cm. The three axes intersect at $z = -15$ cm. The locations of the coils and other components are measured from $z = 0$. The decay channel extends to $z = 35.6$ m, which is the facility interface with the first induction linac. Figures 3.40 and 3.41 show the basic geometry of the facility.

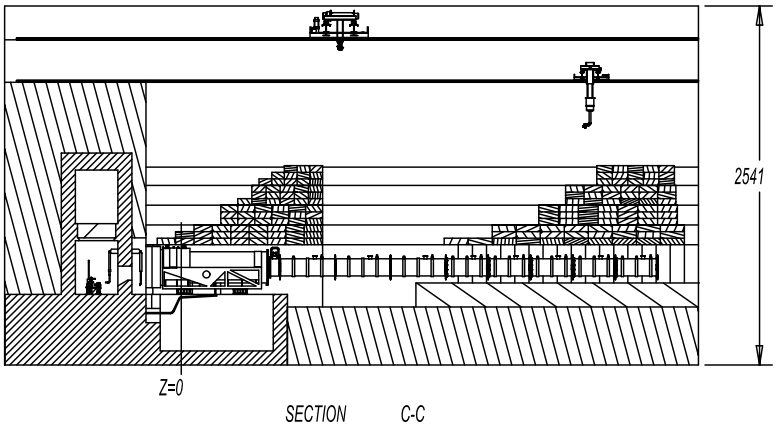

Figure 3.40: Side view of the target facility. Dimensions are in cm.

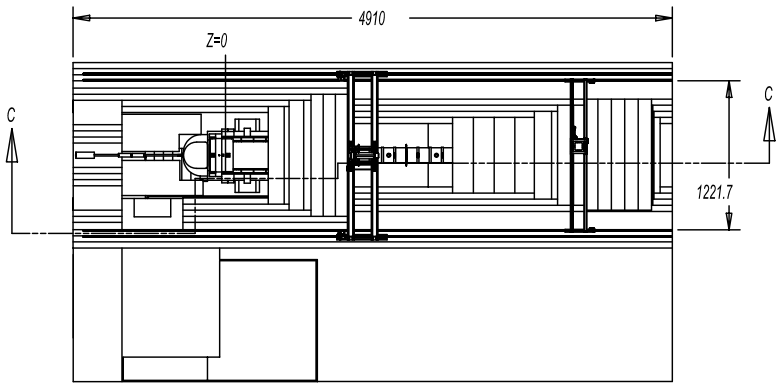

Figure 3.41: Plan view of the target facility. Dimensions are in cm.

The incoming proton beam window is located at $z = -330$ cm and is connected to the core vacuum vessel with a removable section of beam pipe, as shown in Fig. 3.42. This design permits the window assembly to be close to the target region, yet readily

removable to replace the window or the mercury jet nozzle, or provide clearance for the replacement of the inner solenoid module should that ever become necessary.

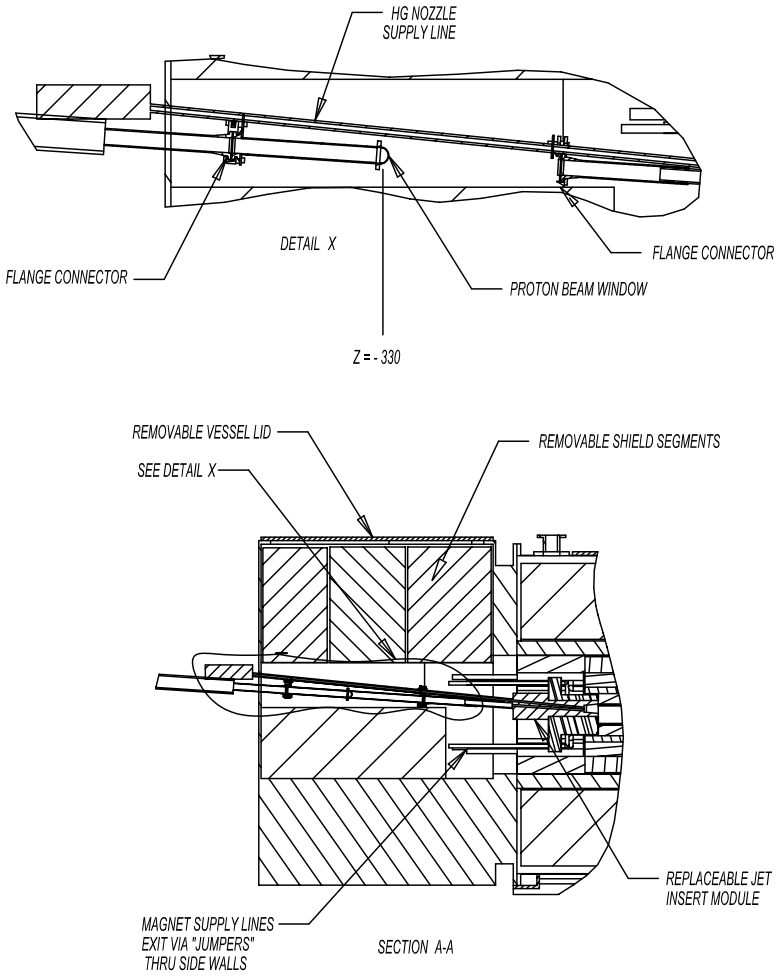

Figure 3.42: Vacuum vessel upstream of the target region.

It is important to keep in mind that virtually all of the components that make up the target and capture facility will be highly radioactive. Replacing components after start-up operations must be done using remote handling equipment and tools. The development of the facility arrangement was based on considering the initial assembly and installation of the various subsystems, and also on modularization of components to simplify remote handling and have minimal impact on the operating availability.

3.8.1 Solenoid Magnets

The solenoid magnets are located in the capture and decay tunnel of the support facility, and although they are considered to be lifetime components, the facility design is based on their remote replacement. The tunnel begins in the target region upstream of the proton beam window and extends to $z = 35.6$ m. The first five solenoids (SC 1–5) are contained in a common cryostat that extends to $z = 6.1$ m. The cryostat is designed so that its inner shell is the outer shell of part of the tungsten-carbide shield. Therefore, there is a shield cylinder attached to the cryostat that is 16-20 cm thick and contains inner rib supports to stiffen this cylindrical beam. The ribs are also partitions for the cooling flow channels of the shield. Figure 3.43 is a section through the main cryostat that shows the magnet arrangement and the shield-beam. Figure 3.44 shows the rib structure of a typical shield module and the coolant line connections.

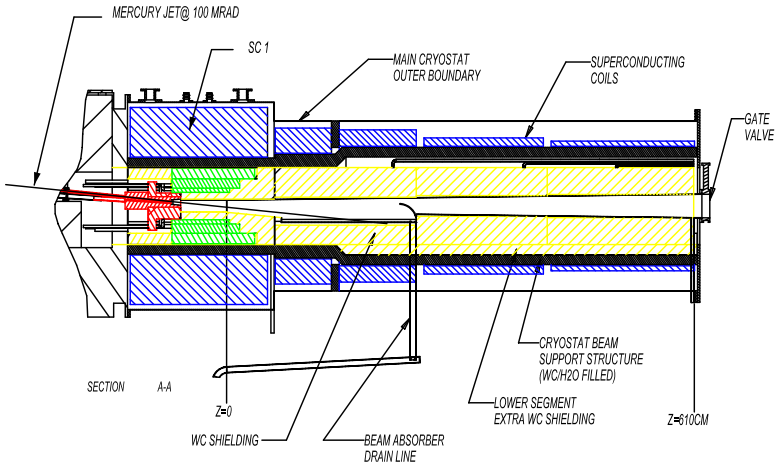

Figure 3.43: Main cryostat containment for SC 1–5.

There is a separate module for the resistive magnets and shielding contained within the bore of SC 1. It consists of an iron plug, three resistive, water-cooled magnets (H-C 1–3), and tungsten-carbide shielding. The combination of these coils and SC 1 provides the 20 T field in the target region. Figure 3.45 shows the resistive coil module along with the nozzle insert for the mercury jet. Figure 3.46 shows a section cut and end view of the resistive module. The target nozzle insert is mounted in the off-center cut-out in the iron plug.

The magnets downstream of the main cryostat are two-coil solenoids contained in 4-m-long cryostats, except for SC 6, which has a 0.5-m cryostat. These magnets extend

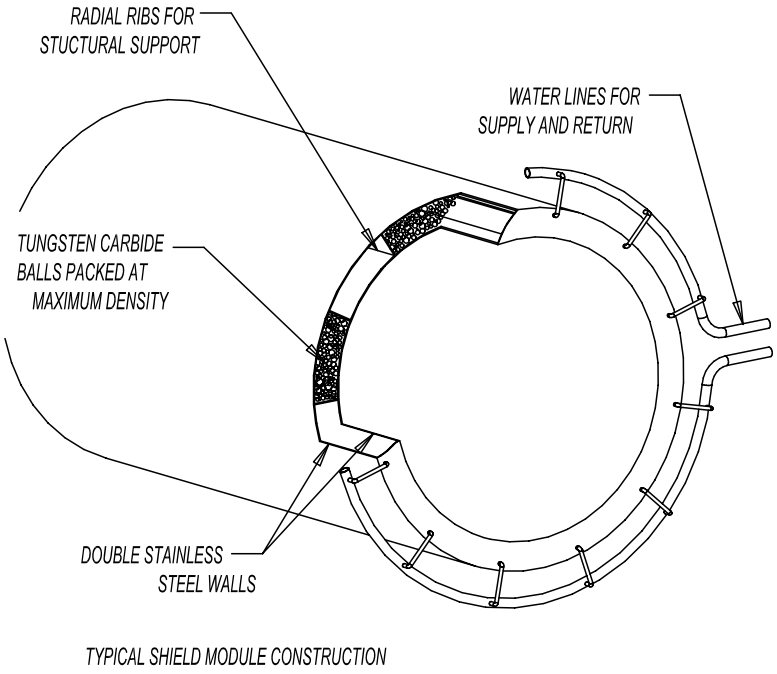

Figure 3.44: Typical construction of the shield modules.

from $z = 6.1$ to 17.6 m and make up the remainder of the transition coils (SC 6–25). Figures 3.12 and 3.39 show the transition coils. In this region, the axial field decreases until it is 1.25 T at $z = 17.6$ m.

Coil SC 6 is smaller and is designed to be the mounting support for the beryllium window located at $z = 6.1$ m. The window is the downstream containment boundary for the mercury target vessel. The window is replaced every two years by removing SC 6 and installing a spare SC 6 module with the replacement window already mounted. Figure 3.39 shows SC 6 in the process of being removed.

The magnets from the end of the transition region to the end of the decay channel are contained in 3-m-long cryostats, each containing three coil pairs. Figure 3.47 is a section- and end-view of a typical cryostat module. The nuclear shielding for these magnets is similar to the upstream coils except that a homogeneous mix of stainless steel balls is used instead of the tungsten carbide balls.

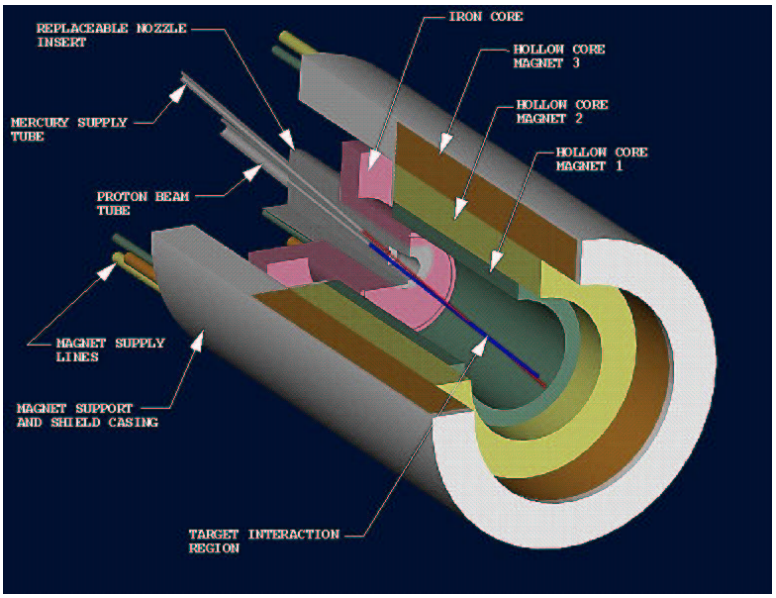

Figure 3.45: Cutaway view of the resistive insert magnets that surround the proton beam and mercury jet.

3.8.2 Assembly and Installation

The assembly and installation of the magnet system was the major consideration for determining the facility arrangement. The coil/shield modules are the heaviest and largest components and were the basis for establishing the building height and width, and determining the crane capacity needed for installation operations and subsequent maintenance.

The overall dimensions of the coil modules and their respective component weights are given in Table 3.16. The largest module weight was used to determine the lifting requirement in the crane hall. Installing the tungsten-carbide shield for SC 4–5 is the heaviest lift at approximately 43 tons. A 50-ton bridge crane with a 46-ft span was chosen.

3.8.3 High-Field Region

The high-field coils providing a 20-T field in the target region comprise three resistive coils (H-C 1–3), an iron plug surrounded by a water-cooled tungsten-carbide shield (Figs. 3.45-3.46), and an outer superconducting coil (SC 1, Figure 3.43). The H-C coils and part of the shield constitute a single module that is installed into the cryostat of the high-field

Table 3.16: Solenoid coil sizes and weights, and shield module weights.

Component	Outer Diam. (cm)	Length (cm)	Module Wt. (lb)
Resistive Module	110	180	47,500
Iron Plug	-	-	-
H-C 1	-	-	-
H-C 2	-	-	-
H-C 3	-	-	-
W-C Shield	-	-	-
Main Cryostat + Shield Beam	270	740	73,600
SC 1	256	178	61,000
SC 2–3	202	183	21,700
Shield 2–3	128	183	59,600
SC 4–5	176	351	17,900
Shield 4–5	148	351	86,400
SC 6 + Shield	104	50	$< 4,000$
SC 7 + Shield	104	185	11,800
SC 8 + Shield	104	185	10,800
SC 9 + Shield	104	185	9,600
SC 10 + Shield	104	185	8,400
SC 11 + Shield	104	185	7,700
SC 12 + Shield	104	185	6,600
Decay Coils + Shield (6)	87	296	12,600

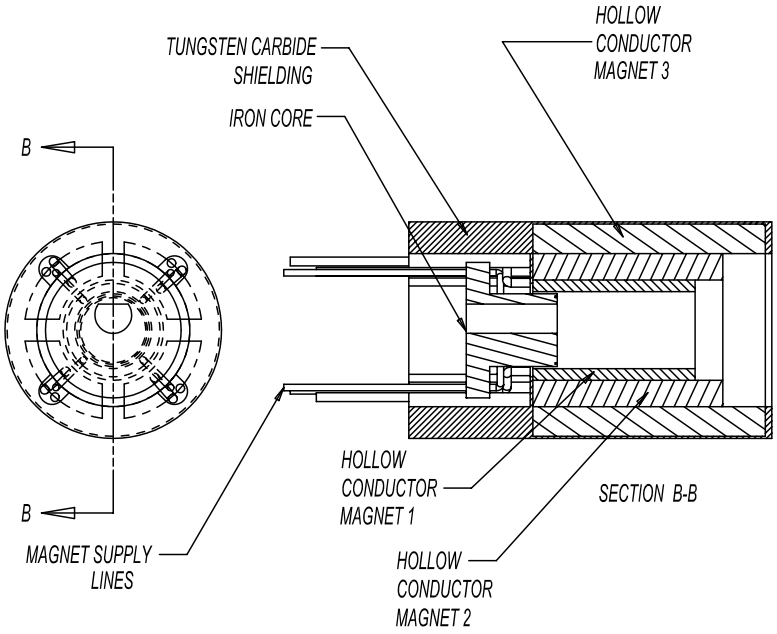

Figure 3.46: Section cut and end view of the resistive coil module.

superconducting coil.

3.8.4 Coil-to-Coil Forces, Method of Support and of Assembly

The net force on coils SC 1–25 is nearly zero, meaning it is a balanced system. SC 1 reacts to the forces of SC 2–25 with an equal and opposite force. However, the coil-to-coil forces between individual magnets are large. SC 1 reacts to the accumulated forces of the downstream coils with 23 million pounds (102.5 kN). The forces from SC 2–5 are, respectively, 1.0×10^6 lb, 6.6×10^6 lb, 3.4×10^6 lb, and 2.3×10^6 lb. (The force contributions from the remaining SC coils are ignored here since they are small by comparison.)

To minimize heat leaks into the SC 1–5 cryostat caused by large-area cold-to-warm-to-cold supports, use of a common cryostat was chosen by the solenoid coil designers. Therefore, the coil-to-coil supports are cold, but the cryostat structure must support the total gravity load of coils SC 1–5. This is accomplished by making a cylindrical portion of the radiation shield part of the cryostat (Fig. 3.43). The cryostat is assembled from two sections onto a continuous cylindrical beam that is part of the radiation shield. The cryostat/beam assembly is lowered into the target region of the tunnel, onto a pair of

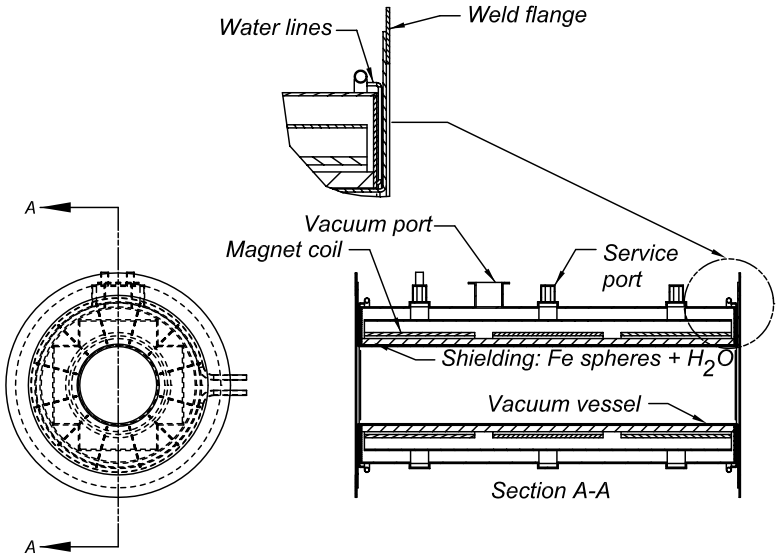

Figure 3.47: Decay channel cryostat module.

trunnion supports (see Fig. 3.48). The trunnion is located midway along the cryostat to minimize the depth of pit area under SC 1–5, and to minimize the elevation of the crane for installing SC 4–5. The cryostat is rotated so that the upstream end points up for the installation of SC 1. The weight of the SC 1 is 61,000 lb. The bridge crane is used to assist lowering the main cryostat so that the downstream end points up and the coil module consisting of SC 2–3 is installed followed by its inner shield. The cryostat is then rotated again, with assistance from the crane, so that the upstream end points up. The resistive coil module (iron plug, H-C 1–3, and shielding) is then installed into the inner bore of the shield-beam. The cryostat position is reversed again and module SC 4–5 is installed, followed by its inner shield. This sequence avoids exceding the 50-ton load limit of the crane. Figure 3.48 shows the installation sequence of the coils in the main cryostat.

3.8.5 Decay Channel Coils

Each of the remaining cryostat modules contains a radiation shield 5-cm-thick, beam mounted to the inner diameter of the cryostat shell. For the coils downstream of $z = 6.1$ m, the shield material is water-cooled copper or stainless steel. A homogeneous mix of stainless steel balls ($2 < d < 6$ mm) is judged to be the most cost-effective approach, and was used for the design.

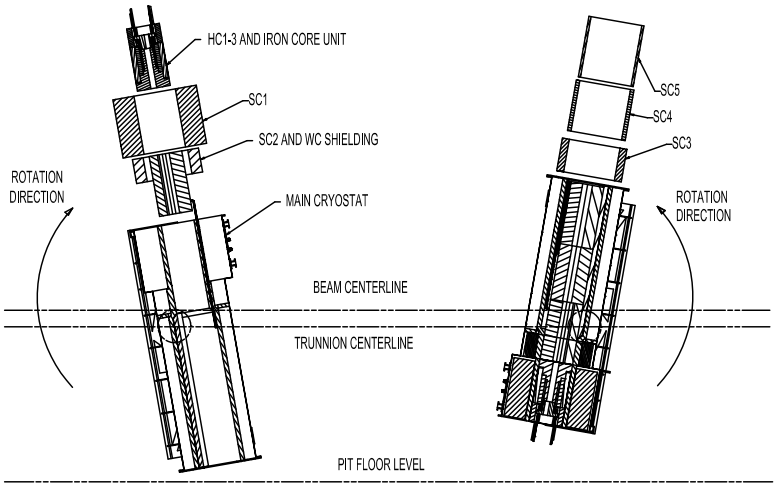

Figure 3.48: Installation sequence for the high field coils SC 1 and H-C 1–3, and transition coils SC 4–5.

A separate vacuum boundary for the muon decay channel is pre-installed to the inner shell of each shield/cryostat assembly. These are assembled so that the outer flange of the vacuum boundary shell can be seal-welded to the flange of adjacent modules, and subsequently cut for disassembly. Figure 3.47 shows typical side and end views of the decay channel magnets, the vacuum flange attachments, and clearance for coolant lines.

3.8.6 Coil Replacement and Remote Handling

The solenoid magnets are designed to be lifetime components. However, they are configured for remote replacement in the event of failure, since they will become highly activated, and since the ability to replace any of them is critical to the operation of the facility. The reverse of the assembly procedure described above is the disassembly method to replace any of the coils. Removal of any solenoid cryostat requires removing at least 24 shield slabs covering the tunnel. Each shield piece weighs 45 tons; ample space has been provided on the crane hall floor to stack the shielding. Once the process of removing shielding is started, personnel access to the crane hall is not permitted and removal operations must be done remotely using the bridge-mounted manipulator system. The maintenance cell located above the target hot cell is configured to accommodate the cryostat modules for subsequent dismantling and waste disposal. The maintenance cell is located adjacent to the staging area where new components are delivered and where

waste disposal casks are shipped out of the facility. Figure 3.49 shows the maintenance cell and its relation to the target region and the staging area.

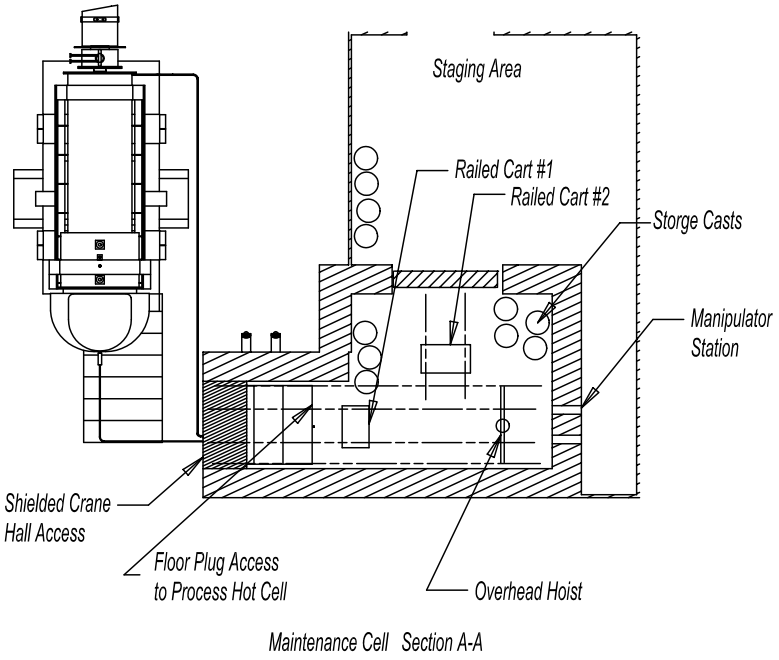

Figure 3.49: The target facility maintenance cell.

3.8.7 Facility Shielding

The facility shielding is designed to permit unlimited access to radiation workers in the crane hall. The shield material and thickness limit the dose rate at the crane hall floor to 0.25 mrem/h (0.0025 mSv). A Monte Carlo neutron, photon, charged particle transport code (MCNPX) using cylindrical geometry was prepared for neutronic calculations. The results show that the shield over the target region should be 5.8 m thick and the shield over the decay channel should be 5.2 m thick. For the purpose of this design, an average thickness was used throughout, consisting of 5.2 m of steel to attenuate fast neutrons and 0.3 m of concrete to attenuate slow neutrons. The model analyzed the shielding requirement downstream to $z = 36$ m, but it is clear that beyond the decay channel, into the first induction linac and beyond, similar facility shielding is needed, and the solenoid components will have dose rates too high to permit hands-on maintenance. Therefore,

the crane hall and the remote handling access that it provides to the target/capture magnets should extend well beyond the end of the decay channel. It may be assumed that the same crane hall configuration could be used to service the linear accelerator regions downstream.

Figure 3.50 is a typical cross section in the decay channel showing the arrangement of removable shield slabs. The dimensions for each shield piece are determined by limiting their weight to 45 tons. The amount of shielding needed to limit the dose rate in the crane hall to 0.25 mrem/h is 5.2 m of steel, covered with a 30-cm concrete layer. Each slab layer is 46-cm thick, but the length and width varies, so each layer has offset joints that avoid a streaming path to the crane hall. It should be noted that the width of the tunnel decreases from 7 m in the target region to 5.2 m at approximately $z = 7$ m because of the smaller diameter of the magnets downstream from SC 7.

The shielding requirement upstream of the target region to attenuate backscattering is 2.6 m of steel. This thickness was chosen to limit dose rate to 1 rem/h. A stacked assembly of steel blocks is located in the 3-m-diameter vacuum vessel that encloses the proton beam window and the mercury-jet nozzle. The beam window is located at $z = -3.3$ m and is attached to the beam pipe feedthrough with a Grayloc© or Reflange© remote connector. (The beam pipe diameter is assumed to be 25 cm, although that is not a limiting factor for the remote connector.) This type of connector is well suited for reliable, robust operations that are done frequently. Figure 3.42 is a section view of the vessel showing the arrangement of the components it contains and the relation with the target system. Removal of the nozzle insert and resistive coil module is through the vacuum vessel after removing shield segments.

3.8.8 Maintenance Operations

The components in the target/capture facility fall into three maintenance categories, as discussed for the target system. The basic maintenance requirements for the facility are summarized in Table 3.17.

3.9 Target System Summary

This chapter has presented conceptual designs of components to generate pions by bombarding a jet of mercury with high-energy protons, and then to capture the pions with a solenoidal field that bends the pion trajectories into helices that fit within the 0.15-m-diameter solenoid bore.

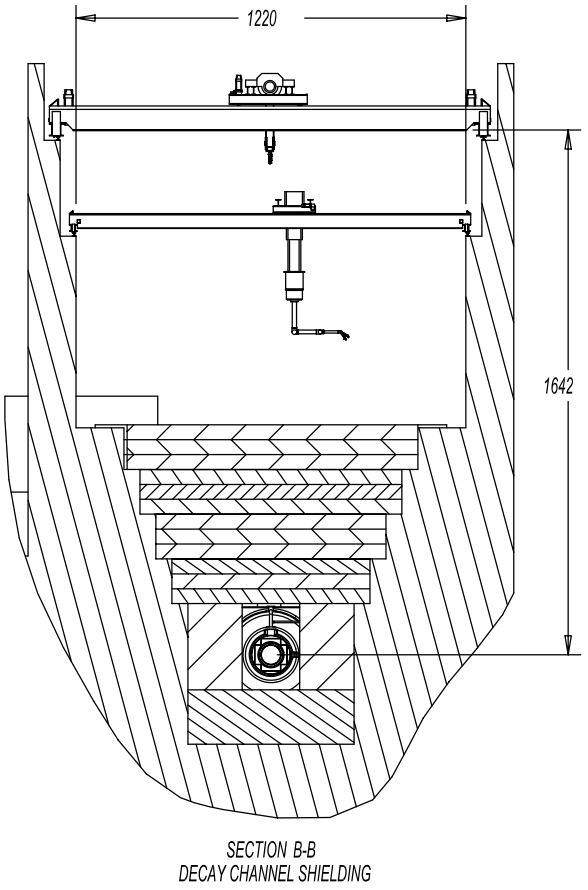

Figure 3.50: Facility shield over the decay channel.

The high-field region is 0.6 m long, with a peak field of 20 T. Downstream the field drops adiabatically by a factor of sixteen to 1.25 T over a distance of 18 m, while the bore increases by a factor of four. The mercury jet is 1 cm in diameter, with a speed of 30 m/s and a tilt angle of 100 mrad relative to the axis of the magnetic field. An analytical estimate predicts that the jet should enter the target region with little deceleration and deflection. However, these calculations suggest that the jet must not encounter any strong field gradient, if it is to avoid excessive shear and distortions in shape. We allow the field to droop only $\approx 5\%$ over the 0.6-m-long target region. Confirmation of the need for field uniformity comes from preliminary results from FronTier, a sophisticated hydrodynamic code that can track the free interface of the jet as it deforms in a magnetic field or breaks

Table 3.17: Maintenance requirements for the target/capture components. The replacement times for the solenoid include the time for fabricate a replacement.

Component	Class	Expected Life (yrs.)	Replacement Time wks.)
Proton beam window	1	2	1
Vacuum pumps, valves, ...	1	7	1-2
Resistive solenoid module	2	> 40	30-40
High-field solenoids	2	> 40	50-60
Transition solenoids	2	30-40 (includes time to > 40	30-40
Low-field solenoids	2	20-30 (includes time to > 40	20-30

up from shock waves.

Finite element analysis predicts that pressure waves from the instantaneous heating of the mercury to several hundred degrees by the proton beam will splatter the jet completely. To replenish the 0.6-m-long jet in only 20 ms, the desired time interval between proton bunches, dictates the 30 m/s jet velocity.

Radiation emanating from the target is intense. The computer code MARS predicts that the neutral flux rate through the beam pipe is up to 3×10^{20} per cm^2 per year for neutrons, and an order of magnitude higher for gamma rays. Charged particle flux rates are 10^{20} per cm^2 per year for hadrons and for electrons. The power dissipation is up to 2 W/g and the total radiation dose up to 4×10^{10} Gy/yr. These levels require shielding of many components, such as the pion capture magnet.

The pion capture magnet system is a hybrid, with many coaxial superconducting coils and a resistive insert. The system stores 600 MJ, with a superconducting coil that generates 14 T in a bore of 1.3 m. The resistive insert receives radiation so intense that only ceramic insulation will survive. The baseline design for the insert uses water-cooled hollow conductor insulated with a layer of magnesium oxide between its copper conductor and sheath. To generate 6 T in a large volume, the coil consumes 12 MW and requires many conductors in parallel in each layer to limit the hydraulic path length. For a design lifetime of many years rather than a few months, the bore accommodates a layer of water-cooled tungsten carbide ≈ 10 cm thick to attenuate the radiation by a factor of 30. The pion capture magnet employs superconducting coils of two types. High-field, large-bore

coils employ cable-in-conduit conductor. The lower-field, smaller-core coils that ramp the field down to 1.25 T employ Rutherford cable (as do the phase-rotation coils farther downstream). All coils require shielding to limit the power deposition to < 1 W/m^3, to avoid quenching, and to limit the radiation dose to < 10 MGy/yr to enable organic insulation to survive.

Additional engineering challenges are mercury containment, mercury jet capture and diffusion, beryllium-window integrity and remote handling. The computer code MCNPX predicts nearly 2 MCi of activation after only a hundred days of operation, with 105 Ci remaining after 30 days of cool-down. The remote handling for maintenance and repair must deal with masses up to 45 tons and with components with limited accessibility. All of these components will benefit from additional research and development. Nevertheless, all aspects of the technology appear feasible.

Bibliography

[1] H.G. Kirk, *Pion Producion Cross Sections from E910 and MARS*, 2nd Intl. Workshop on Neutrino Beams and Inst. (Fermilab, Sept. 6-9, 2000), http://pubweb.bnl.gov/users/kirk/www/e910/fnal00/hkirk.pdf

[2] C.M. Ankenbrandt *et al.*, *Status of Muon Collider Research and Development and Future Plans*, Phys. Rev. ST Accel. Beams 2 081001 (1999)

[3] N.V. Mokhov, *Particle Production for a Muon Storage Ring: I. Targetry and π/μ Yield*, MUC0169 (Sep. 2000), http://www-mucool.fnal.gov/mcnotes/muc0169.pdf

[4] N. Holtkamp and D. Finley, eds., *A Feasibility Study of a Neutrino Source Based on a Muon Storage Ring*, Fermilab-Pub-00/108-E (2000), http://www.fnal.gov/projects/muon_collider/nu-factory/nu-factory.html

[5] B.J. King, N.V. Mokhov, N. Simos and R.V. Weggel, *A Rotating Inconel Band Target for Pion Production at a Neutrino Factory, using Study II Parameters*, MUC0199 (Apr. 9, 2001), http://www-mucool.fnal.gov/mcnotes/muc0199.pdf

[6] R. Samulyak, W. Oh and K.T. McDonald, *Numerical simulation of liquid jets in magnetic fields and applications* (Apr. 3, 2001), http://pubweb.bnl.gov/users/rosamu/www/MHD/Papers/mhd_jets.ps

[7] J. Gallardo et al., *First order perturbative calculations for a conducting liquid jet in a solenoid* (Feb. 21 2001), http://pubweb.bnl.gov/people/palmer/

[8] P. Thieberger, *Estimated perturbations of the axial motion of a liquid-metal jet entering a strong magnetic field*, MUC0182 (Nov. 8, 2000), http://www-mucool.fnal.gov/mcnotes/muc0182.pdf

[9] N.V. Mokhov, *MARS Code System User's Guide*, Fermilab-FN-628 (1995); http://www-ap.fnal.gov/MARS/

[10] N.V. Mokhov, *MARS Code Developments, Benchmarking and Applications*, in *Proc. ICRS-9 Int. Conf. on Rad. Shielding* (Tsukuba, Ibaraki, Japan, 1999), J. Nucl. Sci. Tech. **1**, 167 (2000).

[11] N. Mokhov, *Particle Yield and Radiation Fields in Feasibility Study-2 Target Capture System*, MUC0194 (Mar. 21, 2001), http://www-mucool.fnal.gov/mcnotes/muc0194.txt

[12] MCNPX Users Manual - Version 2.15, L.S. Waters, ed. Los Alamos National Laboratory, TPO-E83-G-UG-X-00001 (1999).

[13] MCNP-A General Monte Carlo N-Particle Transport Code, version 4A, J.F. Breismeister, ed. Los Alamos National Laboratory, LA-12625-M (1993).

[14] R.E. Prael and H. Lichtenstein, *User Guide to LCS: The LAHET Code System*, Los Alamos National Laboratory, LA-UR-89-3014 (1989).

[15] S.A. Fabritsiev et al., *Low-temperature radiation embrittlement of alloys*, J. Nucl. Mat. 233 (1996).

[16] K.H. Tanaka et al., *Development of Radiation-Resistant Magnet Coils for High-Intensity Beam Lines*, IEEE Trans. Magn. **30** (1994).

[17] J. Brooks et al., *World's Most Powerful Magnet Tested*, NHMFL Reports **7:2**, 1 (Spring 2000), http://www.magnet.fsu.edu/publications/reports/spring00screen.pdf

[18] R.J. Jayakumar et al., *The USHT-ITER CS Model Coil Program Achievements*, IEEE Trans. Appl. Supercon. **10:1** (2000).

[19] M.A. Green et al., *Superconducting Solenoids for the Muon Collider*, MUC0162 (Sep. 27, 1998), http://www-mucool.fnal.gov/mcnotes/muc0162.pdf